Efficient Approach for Atmospheric Phase Screen Mitigation in Time Series of Terrestrial Radar Interferometry Data Applied to Measure Glacier Velocity

Yuta Izumi, *Member, IEEE*, Othmar Frey, *Senior Member, IEEE*, Simone Baffelli, *Member, IEEE*, Irena Hajnsek, *Fellow, IEEE*, and Motoyuki Sato, *Fellow, IEEE*

***Abstract*—The accuracy of surface displacements measured by differential radar interferometry is significantly degraded by the atmospheric phase screen (APS). This article presents a practical and efficient approach for APS mitigation based on the coherent pixels technique (CPT) displacement velocity estimation algorithm. In the proposed approach, all motionless coherent pixels closest to the moving area are defined as seeds surrounding the moving area at the integration step of the CPT. This arrangement consequently minimizes the integration path and the APS effect in the final velocity result. It is designed for terrestrial radar interferometry (TRI) applications. A piecewise processing chain is further introduced as a continuous operational mode processing framework to derive arbitrary temporal displacement patterns in this work. Three-day datasets measured by Ku-band TRI over a mountainous region in the canton of Valais, Switzerland, were used for validation. Through this validation, a comparative study of five algorithms was carried out. This evaluation showed the efficiency of the proposed approach. The proposed approach does not require phase unwrapping, kriging interpolation, and spatio-temporal covariance inference for APS mitigation, which is appropriate for continuous TRI operation.**

***Index Terms*—Atmospheric phase screen (APS), glacier, ground-based radar interferometry, radar interferometry, terrestrial radar interferometry.**

Manuscript received March 21, 2021; revised July 3, 2021; accepted July 10, 2021. Date of publication July 27, 2021; date of current version August 16, 2021. This work was supported by Grand-in-Aid for JSPS Research Fellows under Grant 18J20104. *(Corresponding author: Yuta Izumi.)*

Yuta Izumi is with the Institute of Industrial Science, University of Tokyo, Bunkyo-ku 113-8654, Japan (e-mail: yizumi@g.ecc.u-tokyo.ac.jp).

Othmar Frey is with the Department of Earth Observation and Remote Sensing, Institute of Environmental Engineering, ETH Zurich, 8093 Zürich, Switzerland, and also with the Gamma Remote Sensing AG, 3073 Gümligen, Switzerland (e-mail: otfrey@ethz.ch).

Simone Baffelli is with the Laboratory for Air Pollution/Environmental Technology, EMPA, 8600 Dübendorf, Switzerland (e-mail: simone.baffelli@empa.ch).

Irena Hajnsek is with the Microwaves and Radar Institute, German Aerospace Center, 82230 Weßling, Germany, and also with the Department of Earth Observation and Remote Sensing, Institute of Environmental Engineering, ETH Zurich, 8093 Zürich, Switzerland (e-mail: irena.hajnsek@dlr.de, hajnsek@ifu.baug.ethz.ch).

Motoyuki Sato is with the Center for Northeast Asian Studies, Tohoku University, Sendai 980-8577, Japan (e-mail: motoyuki.sato.b3@tohoku.ac.jp).

Digital Object Identifier 10.1109/JSTARS.2021.3099873

I. Introduction

FLEXIBILITY of the terrestrial radars in terms of acquisition timing, mode, and observation geometry can be a major advantage for interferometric measurements on a local scale as compared to spaceborne and airborne synthetic aperture radar (SAR) observations [1], [2]. Displacement estimation with submillimeter accuracy can be achieved using a dense time series of terrestrial radar interferometry (TRI) observations [3].

A wide variety of applications have been reported since 1997 [4]. In most applications, the differential interferometric SAR technique is used to estimate the displacement time series of targets by analyzing a series of TRI images. Those can be roughly categorized into specific purposes: landslide monitoring/prediction [5]–[7], minefield monitoring [8], [9], artificial structure monitoring (building [10], dam [11], bridge [12], tower [13], cultural heritage [14], and monument [15]), and glacier/snow monitoring [16]–[21]. Glacier monitoring addressed in this study is one of the key applications giving essential information for studying its variation as a response to climate change [22] as well as the potential risk detection of the glacier failures for an early warning [16]. Because of the fast-moving and decorrelated characteristics of the glacier, the measurements have been performed in continuous operational mode with a short temporal baseline.

The zero spatial baseline configuration of TRI minimizes several decorrelation sources. Even in this case, artifacts caused by atmospheric refractivity changes between temporally spaced acquisitions known as the atmospheric phase screen (APS) are observed. The APS has been categorized into stratified APS and turbulent APS components [23]–[25] over the mountainous area. The former component is observed in scenarios with vertical stratification of a refractivity index correlated with topography [26], [27]. The latter component, however, is caused by turbulence mixing, exhibiting spatial correlation, described by Kolmogorov's turbulence theory [28]. A detailed analysis can be found in [29].

In these settings, time series interferometric SAR (InSAR) techniques enable reliable land displacement estimation [30]. Many of them share the rationale of the persistent scatterer interferometry [31], [32] and the small baseline subset [33].

Also, the coherent pixels technique (CPT) developed in [34], [35] allows for efficient displacement estimation without the need for spatial phase unwrapping of interferograms. These time series InSAR techniques have also been adapted to TRI processing [36]–[38].

In general, spatio-temporal spectral filtering is used to estimate the APS in these algorithms. In addition, when applied to spaceborne SAR, external auxiliary data such as numerical weather prediction or other remote sensing datasets have been employed [39], [40]. However, such external auxiliary data is not appropriate for TRI applications because of the large spatial scale and relatively lower resolution.

Accordingly, several APS compensation methods for the TRI dataset have been developed. The data-driven model-based statistical approach is a popular method because of its simplicity and does not rely on auxiliary data [41], [42]. Correction of the stratified APS over steep topographic regions for TRI applications was first addressed in [26] and termed a multiple regression model (MRM). Subsequently, the simple linear model of the refractivity index in MRM was modified to take into account heterogeneous refractivity index distribution in [16], [43], [44] by introducing a higher order model. Studies in [45], [46] employed a piecewise regression approach to include a different atmospheric condition along the slant range direction. However, those stratified APS compensation methods cannot fully compensate APS under turbulent atmospheric conditions. The APS caused by turbulent mixing (turbulent APS) and the residual error of stratified APS still substantially impacts the final velocity estimation.

Thanks to the spatial correlation of the turbulent APS [29], the geostatistical kriging approach gives a spatial prediction on displaced locations [16], [43], [47]. The prediction by kriging interpolation is performed using surrounding motionless pixels. As a result, the turbulent APS is possibly corrected by subtracting the predicted APS from the corresponding interferogram. Furthermore, the temporal correlation of the turbulent APS was considered in a recent publication [16]. In specific, temporal correlated nuisance terms are taken into account in the temporal inversion of velocity using generalized least squares (GLS). In this methodology, the covariance of the interferometric error term, which is a superposition of APS and decorrelation phase terms, is explicitly included in the GLS estimator [25]. Although the GLS estimation can give the best linear unbiased estimator, it requires a high computational cost in covariance inference, spatial kriging interpolation, and spatial phase unwrapping. However, such processing is not practically applied to the near-real-time continuous displacement measurement, which requires rapid processing of time series InSAR results.

The presented work proposes applying the CPT algorithm for efficient APS mitigation with an introduced seed-setting strategy as a case study applied to TRI glacier monitoring. We focus on the seed location arrangement at the integration step of the CPT and give a practical approach that selects the multiple seeds around the displaced area. The proposed approach does not have any steps requiring a high computational cost compared to the geostatistical approach. Furthermore, the presented work introduces a piecewise processing chain for the estimation of arbitrary temporal displacement patterns. The evaluation and validation of the presented approach are performed under a controlled simulated environment. Furthermore, the dataset collected by TRI through a glacier measurement campaign is employed to evaluate our method.

The article is organized as follows. Section II introduces the TRI measurement campaign over the glacier in 2015 and hardware specifications. Section III investigates the spatial behavior of the presented turbulent APS in the acquired dataset. Section IV elaborates on the processing chain introduced in this article. Section V demonstrates the proposed APS mitigation approach with the sensitivity analysis by the random field simulation. Section VI presents the velocity estimation results of the acquired TRI dataset estimated by five methods. Finally, some discussions and conclusions are given in Sections VII and Section VIII, respectively.

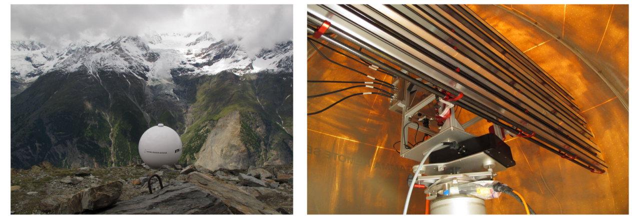

(a) (b)

Fig. 1. (a) Bisgletscher glacier on the opposite side of the valley and the KAPRI sensor covered by a radome. The Bisgletscher shown in the middle of the scene is repeatedly measured from July to August 2015 during a campaign by ETH Zürich [16]. (b) KAPRI in the radome at the test site consisting of six slotted waveguide antennas for fully polarimetric applications.

II. Data: TRI Time Series of a Glacier

The experimental data used in this work is a time series of TRI data of the Bisgletscher, a steep and fast-flowing glacier located on the eastern side of the Weisshorn and Bishorn mountains in the Valais Alps above the village of Randa, Switzerland. The TRI data was acquired using the Ku-band advanced polarimetric radar interferometer KAPRI [48], [49], a fully polarimetric version of the real-aperture Gamma Portable Radar Interferometer [50], from July to August in 2015. The reader is referred to [49] for details on the KAPRI system and [16] for a comprehensive description of the test site and the Bisgletscher TRI measurement campaign.

The Bisgletscher was observed at a 2.5-min time interval to minimize temporal decorrelation and temporal phase wrapping, whereas limited data storage prevented us from selecting an even shorter time interval. The observation was made at an elevation of 2940 m from the Domhütte mountain hut, located on the opposite side of the valley. A photograph taken during this campaign in Fig. 1(a) shows Bisgletscher in the background as well as the radome containing the KAPRI. Fig. 1(b) shows the radar mounted on a pillar inside the radome.

KAPRI is a real aperture radar system based on frequency-modulated continuous wave architecture. The specifications of this radar are shown in Table I (detailed information is available in [49], [50]). The most available ground-based SAR generates

TABLE I
SYSTEM PARAMETERS OF THE KAPRI

Parameter	Value
Center frequency	17.2GHz
Bandwidth	200MHz
Range resolution	0.75m 3dB resolution
Azimuth beamwidth	0.385°
Polarization	HH, HV, VH, and VV

its radar images by synthetic aperture processing by a linear scan of the radar assembly on a rail. In contrast, KAPRI generates the radar images by rotational scanning, lining up the range profile along the azimuth direction without any synthetic aperture processing. The 2-m-long slotted waveguide antennas of the KAPRI have a 0.385° azimuth beamwidth, achieving high azimuth resolution. Operating in the Ku-band frequency range from 17.1 to 17.3 GHz, the range resolution of 0.75 m in the normal distance is achieved. Some calibration steps are required, especially for the polarimetric images, as described in [49].

III. Stochastic Behavior of APS

The atmospheric phase term in an single look complex (SLC) image is defined by the refractivity index $N_{\mathrm{ref}}(r_s, t)$, which is a spatio-temporal function of the temperature, the pressure, and the partial pressure of water vapor [41] at the slant range r_s and the time t, as

$$\phi_{\mathrm{atm}}(t) \; = \; 10^{-6}\frac{4\pi f_c}{c}\int_l N_{\mathrm{ref}}(r_s, t)\, dr_s, \tag{1}$$

where f_c accounts for center frequency, and c is the speed of light. APS can be expressed by taking the difference of two atmospheric phase terms measured at different time t_i and t_{i+1} as

$$\phi_{\mathrm{APS}}\ (t_i, t_{i+1}) = \varphi_{\mathrm{atm}}\ (t_i) - \varphi_{\mathrm{atm}}(t_{i+1}). \tag{2}$$

Based on the physical origin, the APS observed over a mountainous area is categorized into two types of atmospheric signal: $\phi_{\mathrm{APS,str}}$ caused by vertical stratification of N_{ref} and $\phi_{\mathrm{APS,turb}}$ caused by turbulent mixing of heat and humidity within the atmospheric boundary layer (ABL) [51], [52]. The $\phi_{\mathrm{APS,str}}$ component behaves as low spatial frequency and correlates with topography. The model-based approach addresses to estimate $\phi_{\mathrm{APS,str}}$ by approximating the spatial distribution of N_{ref} (see Appendix A).

On the other hand, the $\phi_{\mathrm{APS,turb}}$ component is often stochastically described by variogram, also known as structure-function [51], which describes spatial correlation structure. The variogram is defined by the variance of increment assuming the second-order stationarity of the increment, i.e., the expectation and covariance of increment are assumed not to be dependent on the location [53],

$$\gamma\ (\mathbf{h}) = \ \mathrm{var}\left[\phi_{\mathrm{APS,turb}}(\mathbf{x}+\mathbf{h}) - \phi_{\mathrm{APS,turb}}(\mathbf{x})\right], \tag{3}$$

which is called theoretical variogram, measuring the dissimilarity according to separation $\mathbf{h}$. In practice, experimental variogram is first computed over the high-quality pixels, the so-called coherent pixels (CPs) (see Section IV for CPs detection), by

$$\hat{\gamma}(h_l) = \frac{1}{2N_h(h_l)}\sum_{i=1}^{N_h(h_l)}\left(\phi_{\mathrm{APS,turb}}(\mathbf{x_i}+\mathbf{h}) - \phi_{\mathrm{APS,turb}}(\mathbf{x_i})\right)^2 \quad (\mathbf{h}\in h_l) \tag{4}$$

where N_h is the number of pairs within the given discrete distance h_l. For our data, we assume that the variogram of $\phi_{\mathrm{APS,turb}}$ depends only on the distance, i.e., assuming isotropy of the turbulence.

A parametric variogram model is then fit to the experimental variogram to obtain a continuous variogram. Among several variogram models, this article uses the exponential model for variogram estimation of $\phi_{\mathrm{APS,turb}}$, given as [53]

$$\gamma_{\exp}\ (h) = \sigma^2\left(1 - \exp\left(-\frac{h}{a}\right)\right), \tag{5}$$

where σ^2 is the variance of the process (also known as sill) defined by variogram value at the infinity lag distance, and a is a so-called range of variogram. When $h = 3a$, the exponential model reaches 95% of the σ^2; hence, this distance is called correlation length h_{corr} in this study (also known as a practical range).

Fig. 2(a) shows an example of the mean experimental variogram derived from 22 interferograms observed within 1 h (11:03–12:03, 14th July) as well as a fitted exponential variogram. Note that the stratified APS correction demonstrated in Appendix A is applied to all interferograms to take into account only $\phi_{\mathrm{APS,turb}}$. The derived variogram reveals that selected interferograms have $\sigma^2 = 6.91\ \mathrm{mm}^2$ and $h_{\mathrm{corr}} = 659$ m.

The isotropic turbulence-induced delay has a scale-variant power-law behavior described by Kolmogorov turbulence theory [28], [29], shown as

$$\gamma\ (h) = D^2\,(|\mathbf{h}|)^{\alpha}, \tag{6}$$

where D is the strength of the turbulence and is assumed to be constant over all distances, and exponent α corresponds to the correlation dimension. According to the previous studies in satellite radar interferometry [29], a variogram with a smaller distance than ABL thickness (~2 km) follows the exponent $\alpha = 5/3$, namely 3-D turbulence. In comparison, larger distance than ABL thickness is defined as 2-D turbulence with exponent $\alpha = 2/3$.

Fig. 2(b) shows the mean experimental variogram of three-days interferograms (in total 1404) formed by consecutive SLCs with a 5/3 and 2/3 slope. Although the σ^2 and h_{corr} of experimental variogram temporally vary even within a day due to different solar heating of ground surfaces, we compute three-days averaged variogram to evaluate the general characteristic of the stochastic spatial behavior of $\phi_{\mathrm{APS,turb}}$ over the study area. The computed variogram reveals that the spatial statistics

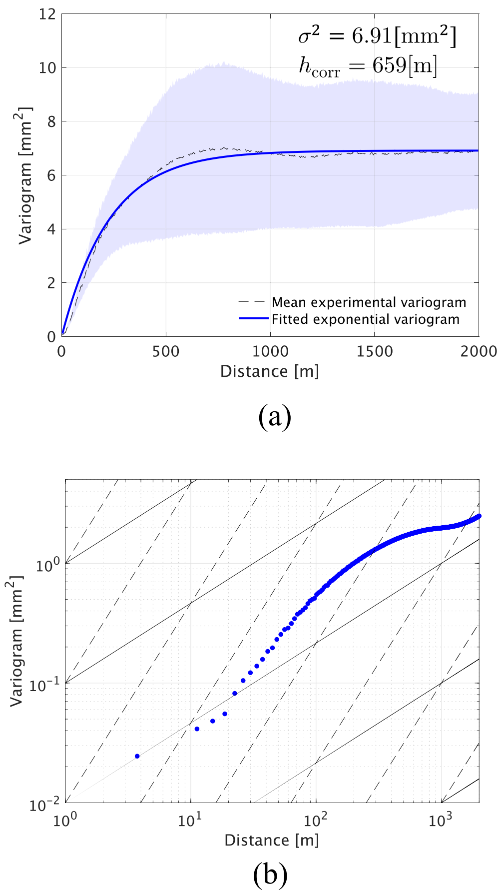

Fig. 2. (a) Mean experimental variogram (dashed line) and fitted exponential variogram model (blue line). The mean experimental variogram is derived from 22 interferograms formed by consecutive SLC images observed within 1 h (11:03–12:03, 14th July). A blue shade represents the standard deviation of the experimental variogram for each spatial lag. (b) Mean experimental variogram of selected three-day interferograms (in total, 1404) acquired from 08:00 13th July to 00:00 16th July. All interferograms are formed between consecutive SLC images with 2.5 min temporal separation. Black solid and dashed lines follow a 5/3 (3-D isotropic turbulence) and a 2/3 (2-D isotropic turbulence) slope.

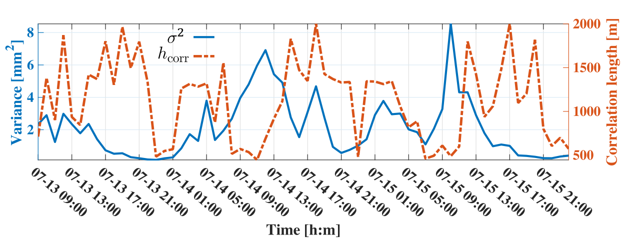

Fig. 3. Time series of σ^2 and h_{corr} derived by corresponding image subset separated each hour (e.g., the result at 09:00 14th July is estimated by images observed from 08:00 to 09:00, 14th July).

of $\phi_{\mathrm{APS,turb}}$ obeys a power-low behavior. Specifically, the variogram in the distance between 10 and 100 m follows a 5/3 slope (3-D isotropic turbulence). It gradually turns out to be a gentle slope and follows a 2/3 slope (2-D isotropic turbulence). Note that such a consequence is expected to be temporally varied. To show the time series variogram information, we plot the σ^2 and h_{corr} of the fitted exponential model derived by the corresponding image subset separated each hour in Fig. 3. Fig. 3 shows a variation of both σ^2 and h_{corr} along the time. At a glance, σ^2 of daytime shows a higher value (more substantial turbulence) than night-time while h_{corr} of daytime shows shorter than that of night-time. Hence, the interferograms acquired during the daytime are much disturbed by turbulence than at night-time, resulting in significant error in displacement estimation.

IV. Methods: Piecewise Processing Chain

The *i*th measured interferometric phase ($\phi^i_{\mathrm{measure}}$) in the zero spatial baseline configuration can be expressed by a summation of displacement phase term, APS (ϕ^i_{APS}), and noise term (ϕ^i_{decorr}), as

$$\phi^i_{\mathrm{measure}}(\mathbf{x}) = \frac{4\pi}{\lambda} T_i v(\mathbf{x}) + \phi^i_{\mathrm{disp,res}}(\mathbf{x}) + \phi^i_{\mathrm{APS}}(\mathbf{x}) + \phi^i_{\mathrm{decorr}}(\mathbf{x}) + 2\pi n, \tag{7}$$

where T_i indicates the time interval between reference and secondary SLC images, $\mathbf{x}$ is a spatial pixel position vector, v accounts for line-of-sight (LOS) surface displacement velocity, and λ is the wavelength of the operational center frequency. The $\phi^i_{\mathrm{disp,res}}$ accounts for a residual phase component of displacement that appears in the case of non-constant velocity (nonlinear displacement).

In near-real-time continuous operational mode, the processing chain needs to permit us the timely update of displacement time series. To fulfill this requirement, we apply displacement velocity estimation to a subset of the dataset; its schematic description is illustrated in Fig. 4. In this processing chain, velocity retrieval is performed when *N* SLC images are obtained, and the processing waits until the following *N* images are available. When we assume a short period (relative to displacement speed) in each time window, $\phi^i_{\mathrm{disp,res}}$ in (7) can be negligible.

A constant velocity value is estimated using a subset of images. Therefore, the processing chain gives the time series of arbitrary displacement patterns by linking all the velocity values, as demonstrated in Fig. 4. Thus, the presented piecewise estimation approach allows for nonlinear displacements occurring at a larger time scale (beyond the time window chosen for the piecewise estimation).

At the beginning of the processing chain, interferograms are formed by means of the selected *N* SLC images with the shortest temporal baseline criterion, referred to as the *daisy chain*. The daisy chain aims to minimize temporal decorrelation and phase wrapping issues along with the temporal domain [54] over the rapidly moving glacier area. For example, with given images acquired at times A, B, and C, we may form interferograms ϕ_{AB} using A and B as well as ϕ_{BC} using B and C, respectively; thus, the number of interferograms *M* equals $N-1$ in the daisy chain.

Before the velocity estimation, a selection of CPs is required to mask noisy pixels. Over the natural distributed area, the temporal mean absolute interferometric coherence criterion lying with the interval [0, 1] is often used [33]–[35], [55] for CPs detection and

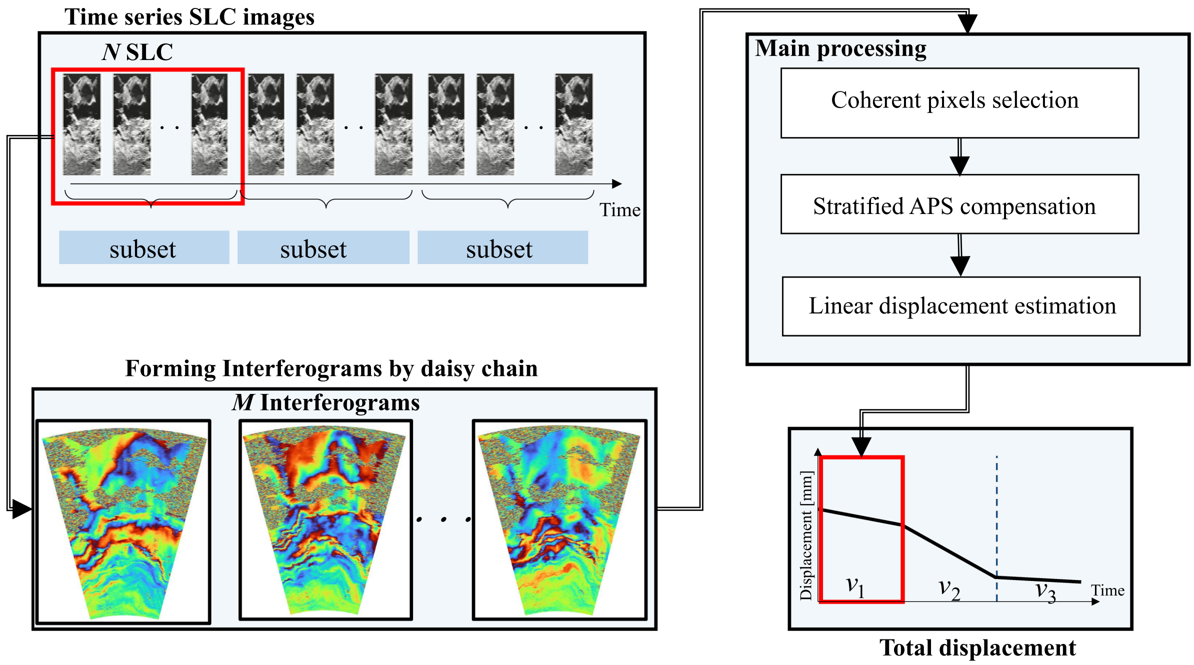

Fig. 4. Piecewise processing chain applied to the series of SLC images.

is defined as

$$\bar{\gamma} = \frac{1}{M} \sum_{i=1}^{M} \left| \frac{\langle s_i s_{i+1}^* \rangle}{\sqrt{\langle s_i s_i^* \rangle} \sqrt{\langle s_{i+1} s_{i+1}^* \rangle}} \right|, \tag{8}$$

where s_i (reference image) and s_{i+1} (secondary image) are complex values corresponding to the same pixel forming an interferogram, and $\langle \cdot \rangle$ indicates the ensemble averaging with the assumptions of both stationarity and the ergodicity realized by spatial averaging. The pixels with higher $\bar{\gamma}$ are then selected as the CPs.

However, the glacier tongue generally shows temporal decorrelation due to the physical displacement and potentially due to temporal changes of the glacier surface properties (e.g., surface moisture change). To illustrate this phenomenon, the coherence variations with respect to the temporal baseline from 0 to 1 h over the glacier tongue are shown in Fig. 5. The red plot indicates the result at a pixel showing the fastest displacement, whereas the blue plot indicates the coherence variation averaged over the glacier tongue. The computed results reveal a rapid coherence drop within 1 h, especially at maximum velocity pixel. According to this fact, the existence of “coherent pixels” seems to be doubtful over the glacier tongue as such regions show strong temporal decorrelation. Nonetheless, we herein assume that the pixels with higher mean coherence than the determined threshold are CPs, in practice. The employed processing defines the interferometric coherence threshold as 0.8 and uses the 7 $\times$ 2 (range $\times$ cross-range) rectangular window for multilook operation.

The stratified APS compensation is carried out for all interferometric pairs using a polynomial atmospheric phase model with respect to slant range and topographic height. The coefficients of this function are determined using an ordinary least-squares

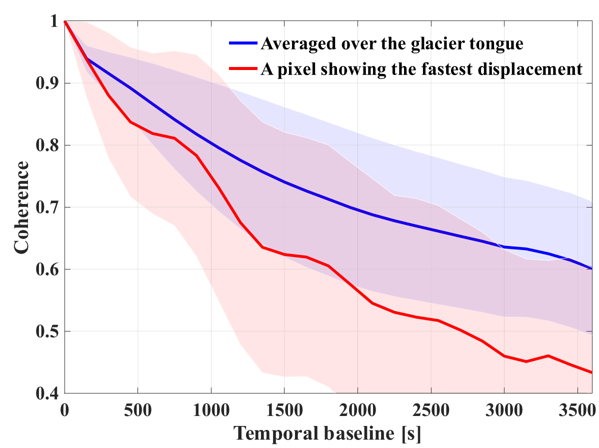

Fig. 5. Coherence variations with respect to temporal baseline. The red plot indicates the result at a pixel showing the fastest displacement, whereas the blue plot indicates the coherence variation averaged over the glacier tongue. Presented results are mean profiles computed by the series of SLC (in total, 547 SLC images are used) obtained from 00:00 14th July to 00:00 15th July. Blue and red shades represent the corresponding standard deviation.

(OLS) solution. The pixels corresponding to the glacier locations should be masked before estimation to avoid biased estimate of the stratified APS parameters. Further details of the stratified APS compensation employed in this study are described in Appendix A.

Finally, velocity estimation is performed by means of interferograms after the stratified APS correction.

V. Methods: Proposed Approach

This section elaborates on the proposed approach based on the CPT algorithm. Section V-A presents the zero-baseline CPT algorithm applied to TRI [36], [38]. A demonstration of the APS effects on the CPT and the multiple-seed approach are described in Section V-B. Section V-C evaluates the presented approach under a simulated environment.

A. Zero-Baseline Coherent Pixels Technique (CPT)

The CPT, developed at the Remote Sensing Laboratory of the Universitat Politecnica de Catalunya (UPC) [34], [35], works with phase increments between spatially separated pixels instead of the absolute phase. In the following, the zero-baseline CPT applied to TRI in [36], [38] is presented in the introduced piecewise processing chain framework.

In practice, Delaunay triangulation relates selected CPs to generate a nonoverlapped spatial triangles network. The interferometric phase increment over an arc between two pixels $\boldsymbol{x}_a$ and $\boldsymbol{x}_b$ is given as

$$\begin{aligned}\Delta\,\phi^i_{a,b} &= \frac{4\pi}{\lambda}\,T_i\left(v\left(\mathbf{x}_a\right)-v\left(\mathbf{x}_b\right)\right)+\left(\phi^i_{\text{error}}\left(\mathbf{x}_a\right)-\phi^i_{\text{error}}\left(\mathbf{x}_b\right)\right)\\ &= \frac{4\pi}{\lambda}\,T_i\Delta v\left(\mathbf{x}_a,\mathbf{x}_b\right)+\Delta\phi^i_{\text{error}}\left(\mathbf{x}_a,\mathbf{x}_b\right), \qquad (9)\end{aligned}$$

where $\Delta\phi^i_{\text{error}}$ is a phase error term after the stratified APS compensation step. This phase error includes the residual APS, temporal decorrelation, and noise component. The residual APS is the term caused by turbulent mixing $\phi_{\text{APS,turb}}$ and an inhomogeneous condition of the atmospheric refractivity.

Once the triangulation is performed over the CPs, velocity increments on all arcs of the network are ready to be estimated. Estimation of velocity increments is performed by minimization of the cost function $\Gamma_{a,b}$ in the complex plane defined as [34], [35]

$$\Gamma_{a,b} \;=\; 2\left(1-\frac{1}{M}\sum_{i\,=\,1}^{M}\text{Re}\left\{e^{-j\left(\Delta\phi^i_{a,b}-\frac{4\pi}{\lambda}T_i\Delta v_{a,b}\right)}\right\}\right). \qquad (10)$$

Through this minimization, the optimal value of $\Delta v_{a,b}$ is estimated in each arc. For computationally efficient and accurate searching rather than brute-force way, the conjugate gradient method (CGM) can be applied [56]. Since the minimization is executed in a complex plane, possible phase wrapping does not impact the model adjustment of phase increments. Therefore, the CPT does not require spatial phase unwrapping.

Once we estimate the velocity increments over the arcs, the phase quality on the arcs is evaluated by the model coherence lying the interval [0, 1] defined in each arc as

$$\gamma^{a,b}_{\text{model}} = \frac{1}{M}\left|\sum_{i\,=\,1}^{M} e^{-j\left(\Delta\phi^i_{a,b}-\frac{4\pi}{\lambda}T_i\Delta\hat{v}_{a,b}\right)}\right|. \qquad (11)$$

In this phase increment estimation step, we may discard the longer arcs to avoid the highly deviated phase increment values [35]. Besides, the arcs with smaller model coherence than a predefined threshold $\gamma^{\text{thres}}_{\text{model}}$ are rejected at this stage. In this article, the model coherence threshold $\gamma^{\text{thres}}_{\text{model}}$ is set as 0.8.

Finally, the absolute velocity at the remaining CPs is obtained through an integration process. For this purpose, the CGM is employed to seek a path-independent global solution [35]. The temporal coherence computed on the arcs will be used in the integration process as the weights through the CGM to reduce the impact of low-quality arcs. The CGM solves the linear equations of the matrix form

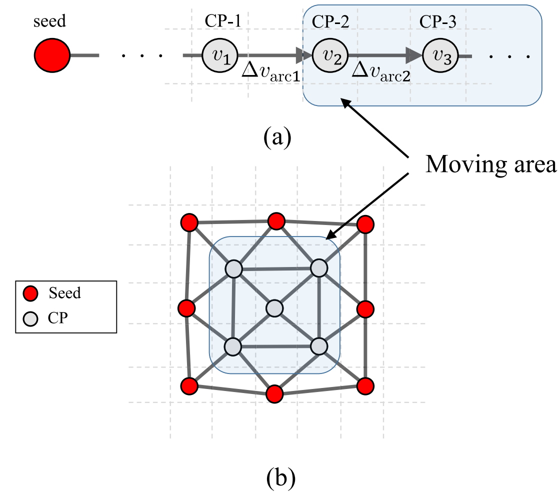

Fig. 6. (a) Example of the 1-D network consisting of CPs and a seed. The blue shade indicates moving area while all the pixels outside of this area are assumed to be motionless pixels. (b) Example of multiple-seed setting strategy. The red and gray circles indicate the seeds and CPs, respectively.

$$\mathbf{W}\mathbf{A}_{\text{arc}}\mathbf{v} \;=\; \mathbf{W}\Delta\mathbf{v}, \qquad (12)$$

where $\mathbf{W}$ is a $[p \times p]$ (p is the number of survived arcs) square diagonal matrix which contains the model coherence, $\mathbf{A}_{\text{arc}}$ is a $[p \times q]$ (q is the number of survived CPs) incidence matrix defining the relationships between CPs and arcs, $\mathbf{v}$ is a $[q \times 1]$ vector of unknown absolute velocity values, and $\boldsymbol{\Delta}\mathbf{v}$ is a $[p \times 1]$ vector of velocity increments. $\mathbf{A}_{\text{arc}}$ consists of -1, 0, and 1 for each row with -1 and 1 for corresponding CPs and 0 for the rest. However, the system in (12) is underdetermined because the matrix $\mathbf{A}_{\text{arc}}$ is singular. Therefore, the velocity of pixels with known displacements called *seed* is fixed in (12). For this purpose, all columns of $\mathbf{A}_{\text{arc}}$ associated with selected seeds are set to 0, and the known absolute velocity values (usually 0) are added or subtracted from $\boldsymbol{\Delta}\mathbf{v}$ [57]. We typically select stable areas unaffected by displacement as the location of the seeds (in this case, the ones outside of the glacier area). The estimated absolute velocity values by the integration process with CGM on survived pixels are the outcomes of the CPT.

B. Multiple-Seed Selection Approach

An impact of the residual APS effect in the CPT is herein demonstrated. We focus on the seed location arrangement at the integration step of the CPT and propose an effective seed setting strategy to minimize the APS effect on final velocity estimation.

Fig. 6(a) describes an example of the 1-D network consisting of CPs and a seed. A blue shade indicates a moving area, while all the pixels outside of this area are assumed to be motionless pixels. Let us consider the velocity estimation of CP-3 in Fig. 6(a) at an integration step. The absolute velocity on

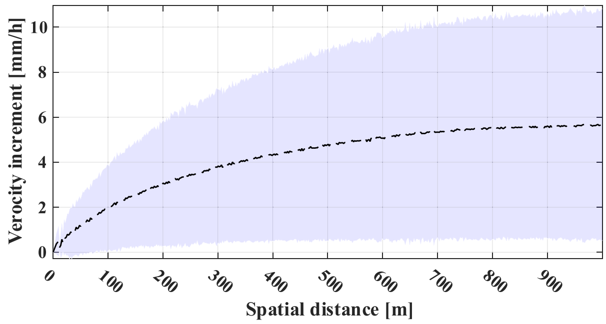

Fig. 7. Mean velocity increment with respect to relative spatial distance between motionless CPs located outside of glacier. The interferograms acquired from 00:00 14th July to 00:00 15th July are used for averaging. All interferograms are formed by SLCs separated by 2.5 min. The blue shade represents the standard deviation.

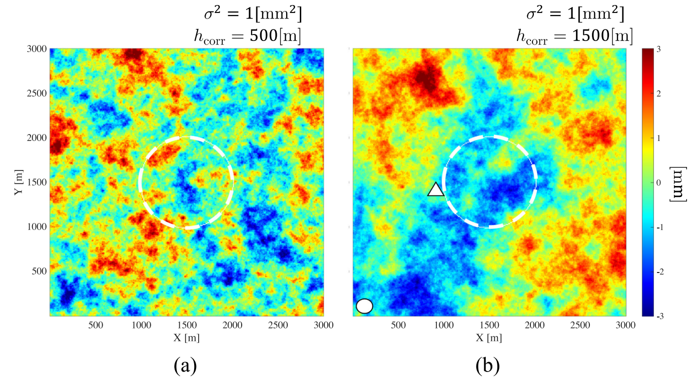

Fig. 8. Examples of 2-D isotropic zero-mean Gaussian random fields, simulating the turbulent APS. A white dotted open circle indicates the estimation area for the evaluation. A white filled circle and a triangle indicate the locations of the seed for CPT-SF and CPT-SC, respectively. (a) $h_{\mathrm{corr}} = 500$ and $\sigma^2 = 1$. (b) $h_{\mathrm{corr}} = 1500$ and $\sigma^2 = 1$.

CP-3 can be obtained by

$$\hat{v}_3 = v_1 + (\Delta\hat{v}_{\mathrm{arc1}} + \Delta\hat{v}_{\mathrm{arc2}}), \tag{13}$$

where the weights are neglected for simplification of this example. The expression in (13) implies two error propagation effects of the residual APS.

The first effect is the APS propagated due to the integration of $\Delta\hat{v}_{\mathrm{arc1}}$ and $\Delta\hat{v}_{\mathrm{arc2}}$. Such a velocity increment $\Delta\hat{v}_{\mathrm{arc}}$ may contain phase error terms, including residual APS in addition to displacement velocity increment; hence, we can write

$$\Delta\,\hat{v}_{\mathrm{arc}} = \Delta v_{\mathrm{disp}} + \Delta v_{\mathrm{APS,res}}. \tag{14}$$

The error propagation effect can be minimized when both CP-1 and CP-3 share a similar atmospheric disturbance. This assumption is usually acceptable if both pixels are spatially close and show a similar temporal APS behavior, corresponding to high spatial correlation. To display this phenomenon using the real TRI dataset, we plot the estimated velocity increment values with respect to the relative distance between CPs in Fig. 7. Because we only use motionless pixels outside the glacier tongue, the velocity increment in Fig. 7 shows only the atmospheric noises. Fig. 7 reveals that the APS velocity increment increases as relative distance increases. According to this fact, the amount of APS error is related to the path distance. This is because the spatial correlation between CPs decreases as relative distance increases.

The second effect is the APS on v_1 caused by APS integration along a prior path between the seed and the CP-1 as well as the APS effect on the seed. A significant APS effect is expected in case of a longer integration path between the CP-1 and the seed. Nonetheless, CP-1 can be a seed pixel with the knowledge of the actual displacement velocity value at the CP-1 [$v_1 = 0$ for an example in Fig. 6(a)]. By doing so, a column of $\mathbf{A}_{\mathrm{arc}}$ associated with the CP-1 is set to 0, equivalent to $v_1 = 0$ in (13). In this way, the APS effect at v_1 can be avoided, and only the integration of $\Delta\hat{v}_{\mathrm{arc1}}$ and $\Delta\hat{v}_{\mathrm{arc2}}$ will impact on $\hat{v}_3$ estimate.

To sum up, motionless CPs closest to the estimation pixels better be selected as the seed pixel to minimize the APS effect at the integration step. A shorter integration path between a seed and pixels of interest is preferable for an APS mitigation.

Let us expand the 1-D example to the 2-D practical case shown in Fig. 6(b). According to the conclusion of the 1-D case, we introduce a multiple-seed arrangement to minimize the APS effects at the integration step. All motionless CPs closest to the moving area are defined as seeds surrounding the moving area, as illustrated in Fig. 6(b). Consequently, this multiple-seed strategy minimizes the physical distance between seeds and pixels of interest toward mitigating the residual APS effect in final absolute velocity results.

C. Evaluation and Sensitivity Analysis

An evaluation and a sensitivity analysis of the multiple-seed strategy are performed under a simulated environment. 2-D isotropic zero-mean Gaussian random fields are generated with corresponding covariance matrices given by variogram [58], [59] to simulate the turbulent APS effect. For this purpose, we use the software package "RandomFields" written in the R language [60]. The exponential model is employed with varying correlation length h_{corr} and variance σ^2 for this simulation. We simulate the turbulent APS on 300×300 pixels where each pixel is assumed to be $10 \times 10\ \mathrm{m}^2$. Fig. 8 shows examples of produced random fields with different correlation lengths (Fig. 8(a): $h_{\mathrm{corr}} = 500$ and $\sigma^2 = 1$; Fig. 8(b): $h_{\mathrm{corr}} = 1500$ and $\sigma^2 = 1$).

We produce 24 interferograms for an interferogram stack. The velocity estimation is performed over the area inside a white dotted open circle indicated in Fig. 8. Note that we randomly select 30000 pixels out of 90000 pixels as CPs in this test. To evaluate the estimated velocity error with respect to seed location and the number of seeds, three types of approaches are applied and compared: 1) CPT with multiple seeds surrounding the estimation area (CPT-M), 2) CPT with a single seed located far from the estimation area (CPT-SF), and 3) CPT with a single seed located close to the estimation area (CPT-SC). Seed locations of both CPT-SF and CPT-SC are indicated by a white filled circle and triangle symbols in Fig. 8(b), respectively. Furthermore, for the sensitivity analysis, we vary σ^2 from 0.1 to 8 mm^2 with an increment of 0.1 as well as h_{corr} from 500 to 2000 m with an

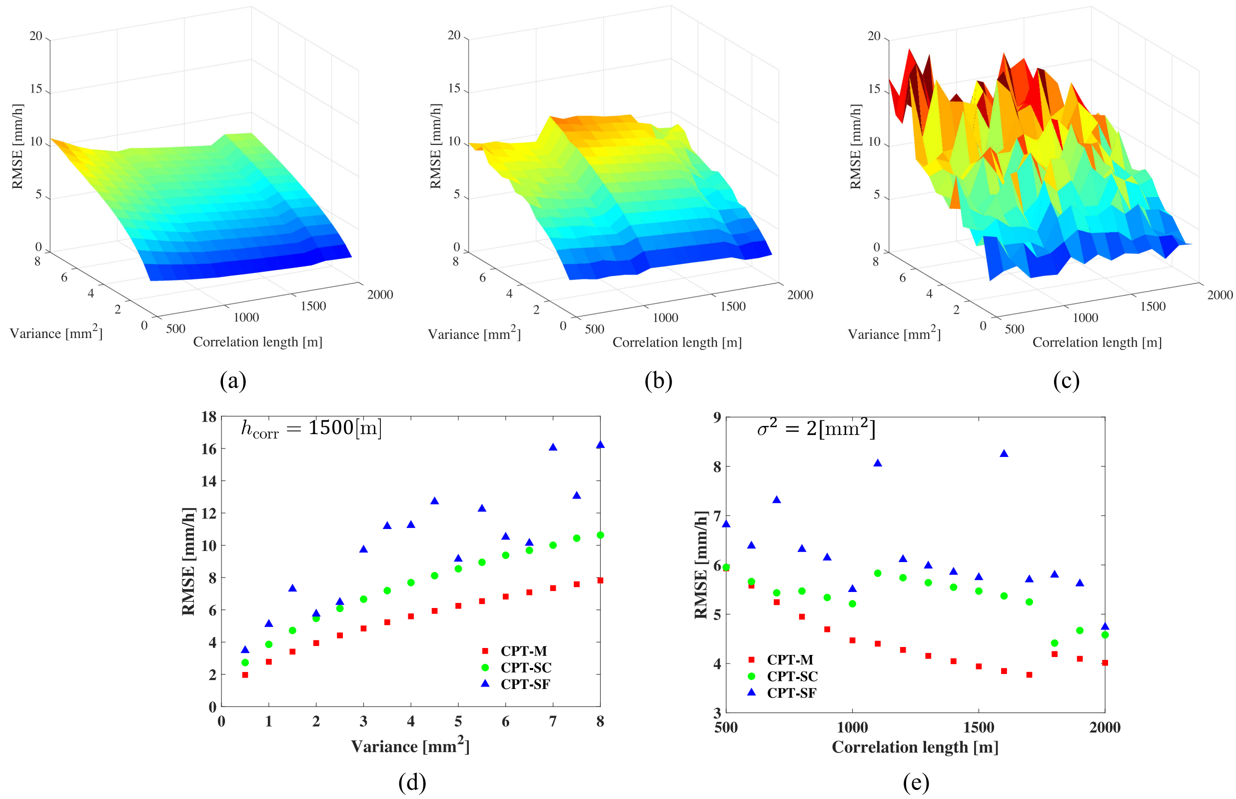

Fig. 9. RMSE value of the retrieved velocity over the estimation area with respect to σ^2 and h_{corr} for three approaches. (a) CPT-M. (b) CPT-SC. (c) CPT-SF. (d) 2-D slice at $h_{\text{corr}} = 1500$ m. (e) 2-D slice at $\sigma^2 = 2$ mm^2.

increment of 100. Those ranges of two parameters are almost equivalent to the statistics of our dataset revealed in Fig. 3.

Fig. 9 shows the root-mean-square-error (RMSE) of retrieved velocity over the estimation area (actual displacement velocity value is 0 mm/h). For the comparison in a different view, we display 2-D plots of Fig. 9(a)–(c) with fixed h_{corr} or σ^2 in Fig. 9(d) and (e).

Comparing the CPT-SF and the CPT-SC, the CPT-SC yields lower RMSE than the CPT-SF. Also, the result shows a strong fluctuation of RMSE in the CPT-SF plot. According to the result, a better estimate with respect to atmospheric turbulence can be achieved by placing a seed as close as possible to the area of interest. Comparing the CPT-M and the CPT-SC, the CPT-M yields lower RMSE than the CPT-SC. This fact reveals that the multiple-seed setting can minimize overall RMSE on final velocity outcome because integration paths between the estimation pixels and seeds become shorter. Furthermore, general trends of the three approaches reveal that when the σ^2 becomes higher as well as h_{corr} becomes shorter, RMSE approaches a higher value. The maximum RMSE value of CPT-M results in 10.8 mm/h when $\sigma^2 = 8$ and $h_{\text{corr}} = 500$ for this simulation.

VI. Experimental Results

The performance of the proposed approach was tested with a TRI HH-polarization dataset described in Section II. The processing chain presented in Section IV was applied to the 3-day time series dataset from 08:00 CEST 13th July to 00:00 CEST 16th July obtained through the glacier observation campaign. Although the TRI acquired images with 2.5 min time intervals, some interferograms were formed with more than 5-min temporal separation because of missing or incorrectly processed images. We rejected such interferograms in this analysis.

The main purpose of this section is to provide the velocity estimation results of five approaches for relative comparison in terms of accuracy, robustness, and computational time that will be discussed in Section VII. In addition to CPT-SF, CPT-SC, and CPT-M, pixel-wise velocity inversion methods with geostatistical approaches are applied as the conventional methods that can mitigate the residual APS, applied in [16]. The terminology of the additional two methods and the explanations are described as follows. Appendix B elaborates on further details of both approaches.

1) OLS-Kriging

The OLS is applied to the absolute phase system in (21) for pixel-wise velocity inversion, as expressed in (22). Kriging spatial prediction is performed over the moving area, applying to all interferograms before OLS inversion. The predicted turbulent APS by kriging is subtracted from the corresponding interferogram to correct APS. Simple kriging in (26) is selected as one of the kriging methods. The kriging system uses the nearest 400 neighbor CPs outside of the glacier (CPs considered to have zero displacements within the timespan of interest) to any prediction pixels.

2) Generalized least squares

The GLS is applied to the absolute phase system in (21) for pixel-wise velocity inversion, as expressed in (23). The covariance of the interferometric error term, which is a superposition

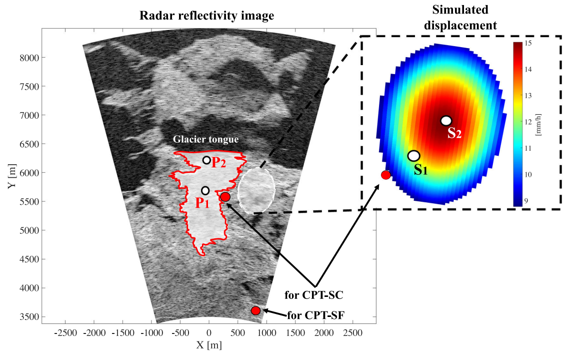

Fig. 10. Locations of the simulated displacement and the glacier tongue indicated by white and red borderlines, respectively. A linear displacement with the maximum velocity of 15 mm/h is added beside glacier tongue. The spatial extent is expressed by a 2-D Gaussian function. S_1 and S_2 represent the locations of investigation pixels for synthetic dataset. P_1 and P_2 indicate the locations of investigation pixels for test on the glacier. The red-filled circles indicate the locations of seeds for the CPT-SF and the CPT-SC.

of APS and decorrelation phase terms, is explicitly included in the GLS estimator. Simple kriging-based APS correction is applied to all interferograms before inversion, similar to the OLS-Kriging.

Because both the OLS-Kriging and the GLS implement a kriging-based correction, estimation results are expected to have less APS contribution than the one without kriging with a price of the computational time.

Note that the CPT does not apply the 2-D spatial phase unwrapping operation. On the other hand, the OLS-kriging and the GLS perform 2-D-phase unwrapping to make the system in (21) linear using minimum cost flow algorithm [61] by GAMMA software. This aspect is related to computational cost.

A Validation With the Synthetic Data

First, the performance of the five methods was evaluated using synthetic dataset with simulated displacement. Displacement with a maximum velocity of 15 mm/h (positive sign corresponds to the direction from the target to the TRI) was added to the measurement data synthesized besides the glacier zone, as indicated by the white borderline in Fig. 10. The simulated location was carefully selected over the stable area (bare surface) outside the glacier tongue. Since we know the actual velocity of the simulated displacement, the RMSE was used as an estimation quality measure. The seeds' locations for CPT-SF and CPT-SC are indicated in Fig. 10.

Employing the three-day dataset from 08:00 13th July to 00:00 16th July, 64 image subsets in total were obtained by the piecewise processing chain; hence, 64 corresponding velocity maps were produced. Fig. 11 exhibits the RMSE maps for five methods derived from all 64 velocity maps. Those reveal the non-uniform distribution of the RMSE value. The CPT-SC shows that closer to the seed location, lower RMSE was yielded. The CPT-M, OLS-Kriging, and GLS show higher RMSE values around the center part of the simulated area than the outer part. The scatter plots of actual velocity versus estimated velocity for

TABLE II
RMSE Values of Five Methods at S_1 and S_2

Point	RMSE [mm/h]				
	CPT-SF	CPT-SC	CPT-M	OLS-Kriging	GLS
S_1	4.53	2.39	2.15	1.95	1.76
S_2	4.58	3.91	3.14	3.77	3.65

five methods are plotted in Fig. 12 with corresponding RMSE and R^2.

Fig. 13 presents the time series of two points to show the temporal behavior of both locations, i.e., the center point S_1 and the outer point S_2, indicated in Fig. 10. In Fig. 13, the time series velocity values were derived by the corresponding image subset (e.g., the result at 09:00 14th July is estimated by images observed from 08:00 to 09:00 14th July). Table II tabulates the RMSE values of five methods at both S_1 and S_2.

B Test on Glacier

The performances of the five methods were evaluated over the glacier tongue indicated by the red borderline in Fig. 10. Fig. 14 displays examples of the LOS velocity map for five methods. The residual APS effects remained in the CPT-SF and the CPT-SC results, where the negative velocity caused by APS can be seen in Fig. 14(a) and (b). As visually confirmed, such APS effects were successfully corrected in the CPT-M and geostatistical methods. Fig. 15 displays the velocity maps of five methods averaged over 64 velocity images. Because we applied an averaging operation along the temporal axis, the APS errors in final velocity results are minimized. Thus, all methods result in a similar spatial velocity pattern, but the averaging operation sacrifices time series variability. From those figures, we visually confirm that the top part of the glacier shows a higher velocity than the bottom part. This conclusion agrees with estimates of the Bisgletscher displacement speed obtained by the offset tracking method on radar amplitude images [62].

Fig. 16 shows the standard deviation (SD) of the estimated velocity maps for five methods to visualize the robustness of retrieval. In total, 64 velocity maps were used for the derivation of the SD. The CPT-SC reveals the lower SD around the seed than pixels far from the seed, which is a similar phenomenon shown in Fig. 11(b).

Furthermore, the velocity time series of two locations at P_1 and P_2 indicated in Fig. 10 are given in Fig. 17 for the in-depth visualization of estimated velocity temporal behavior.

VII. Discussion

This section provides itemized discussions of the results presented in Section VI. The applicability of the CPT-M is discussed by comparing its performance with the other four methods. The comparison among the CPT-M, CPT-SF, and CPT-SC is described in Section VII-A. The comparison between the CPT-M and geostatistical approaches is given in Section VII-B.

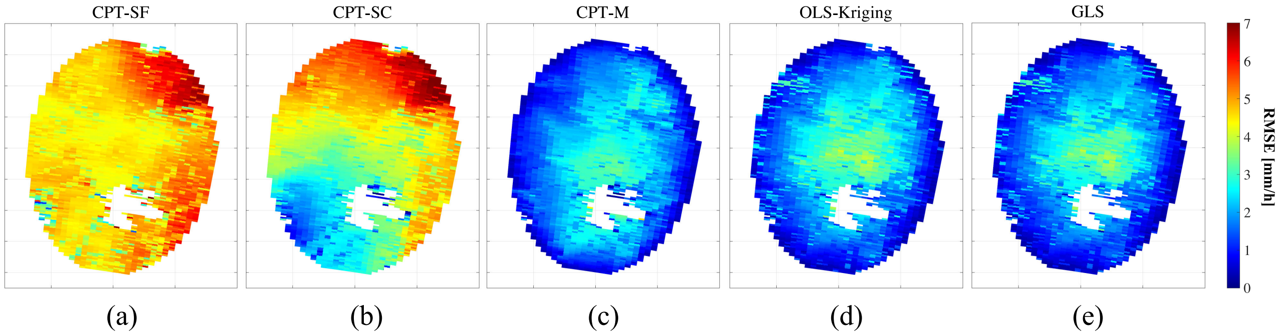

Fig. 11. RMSE maps derived by 64 velocity results (from 13th July to 15th July) over the simulated displacement pixels. (a) CPT-SF. (b) CPT-SC. (c) CPT-M. (d) OLS-kriging. (e) GLS.

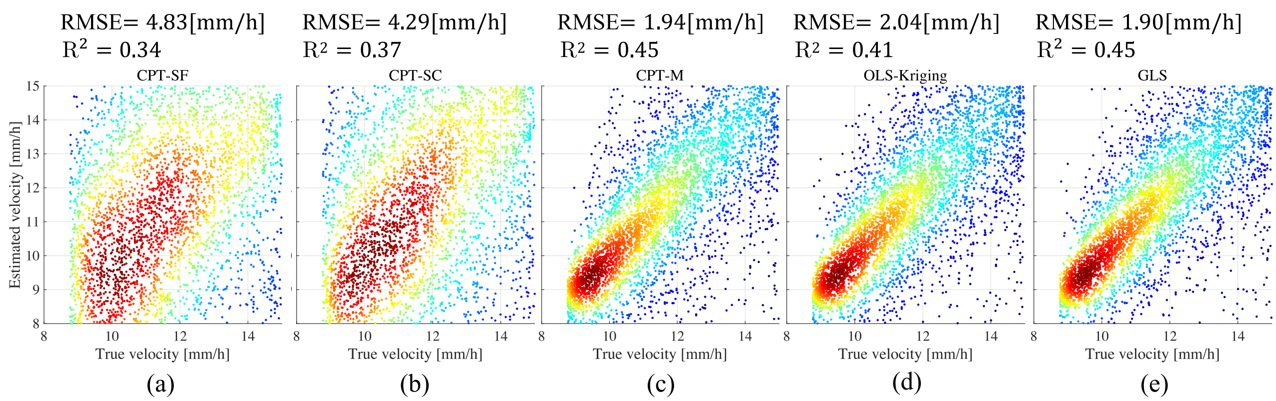

Fig. 12. Scatter plots of the true velocity versus the estimated velocity over the simulated displacement location. Corresponding RMSE and R^2 values are drawn at the top of each figure. Color represents the density of plots (the number of plots for each figure is restricted to 10 000 for the clear visualization purpose). (a) CPT-SF. (b) CPT-SC. (c) CPT-M. (d) OLS-kriging. (e) GLS.

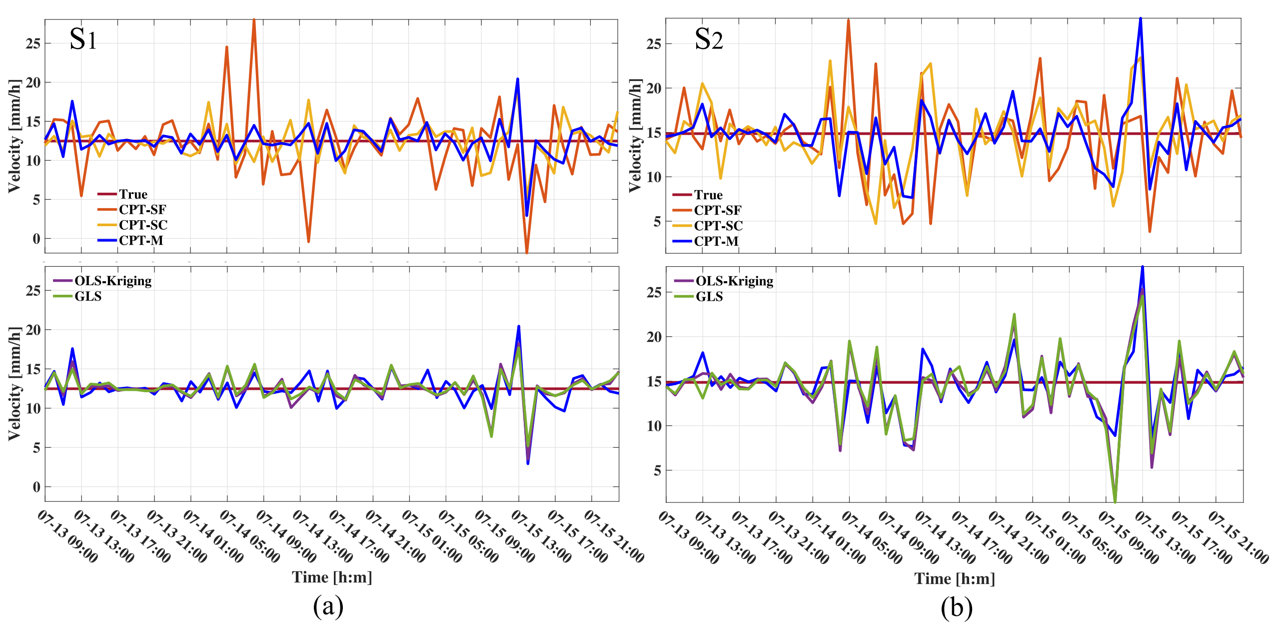

Fig. 13. Time series plots of LOS-simulated displacement velocity at selected two pixels (S_1 and S_2). The constant velocity values are retrieved by a subset of images within 1 h. The top figures show the results of CPT-SF, CPT-SC, and CPT-M. The bottom figures show the results of CPT-M, OLS-kriging, and GLS. True velocity is plotted as red color. (a) S_1. (b) S_2.

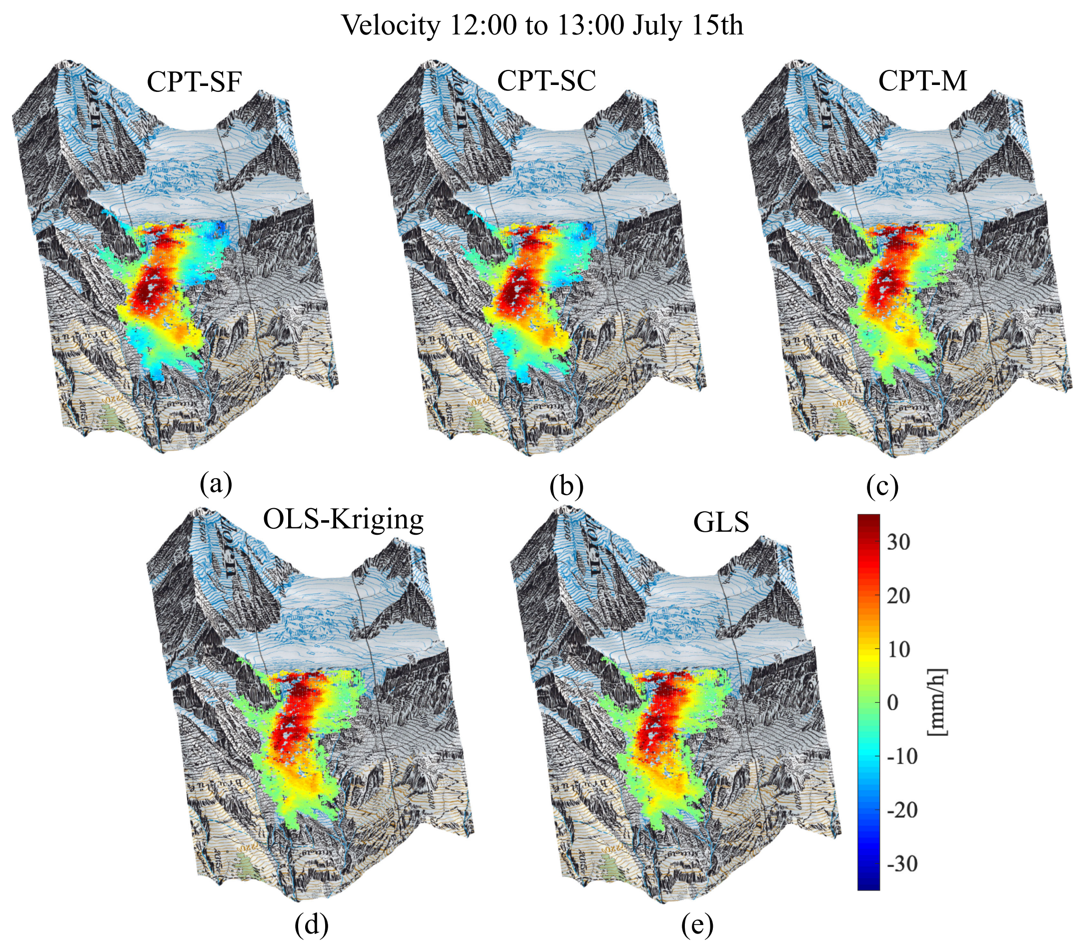

Fig. 14. Examples of LOS velocity derived by TRI images from 12:00 to 13:00, 15th July. The velocity outcome is plotted as a geocoded map overlaid on a topographic map. (a) CPT-SF. (b) CPT-SC. (c) CPT-M. (d) OLS-kriging. (e) GLS.

A. Comparison With CPT-SF and CPT-SC

From the RMSE of the simulated displacement shown in Fig. 11, a noticeable improvement is seen in the CPT-M, compared to the two methods. Fig. 11 reveals significant impacts of residual APS effects on final velocity results in the CPT-SF and the CPT-SC cases. The scatter plot of the CPT-M in Fig. 12 shows the lowest RMSE and highest R^2. Diffuse scatter plots in the CPT-SF and the CPT-SC visually indicate the residual APS influences. Also, the CPT-M presents the velocity time series with less error than the other two methods in Fig. 13. Table II demonstrates that the CPT-M yields the lowest RMSE values at both S_1 and S_2.

The above consequences also appear in results over the glacier tongue. Fig. 16 shows that the CPT-M yields the lowest SD over the glacier tongue. Similarly, the CPT-M gives the velocity time series with less fluctuation than both CPT-SF and CPT-SC, as shown in Fig. 17. These results prove the robustness of the CPT-M against atmospheric disturbances.

The obtained results indicate that the multiple-seed-setting approach effectively mitigates the residual APS at the integration step. Consequently, the CPT-M yields higher accuracy than the single-seed arrangement without increasing the computational cost.

B. Comparison With Geostatistical Mitigation Approaches

A high computational burden in spatial kriging interpolation applied to all interferograms should be considered for the OLS-kriging and the GLS. In addition to kriging, the GLS requires the inference of covariances $\mathbf{\Sigma}_{\mathrm{atm,t}}$ and $\mathbf{\Sigma}_{\mathrm{decorr}}$ by all possible pairs of phase unwrapped interferograms for better estimation, requiring an additional computational cost. In contrast with the geostatistical methods, the CPT-M does not require such high computational processing. In a big O notation, the computational time of the CPT-M is $O(q)$, where q is the number of velocity estimation pixels. On the other hand, the geostatistical approaches require $O(qn^3)$, where n is the number of neighbor pixels (motionless CPs) used for weights determination and weighted average in (26) at kriging interpolation. Nonetheless, according to the results, the estimation accuracy of the CPT-M seems to be very similar to both the OLS-kriging and the GLS.

From Fig. 11, we recognize that the CPT-M shows the RMSE image almost equivalent to the other geostatistical methods over the simulated region. Accordingly, the scatter plots and corresponding RMSE and R^2 of the CPT-M in Fig. 12 are almost accordant with the others. This fact is confirmed in tabulated RMSE values in Table II for both S_1 (center part)

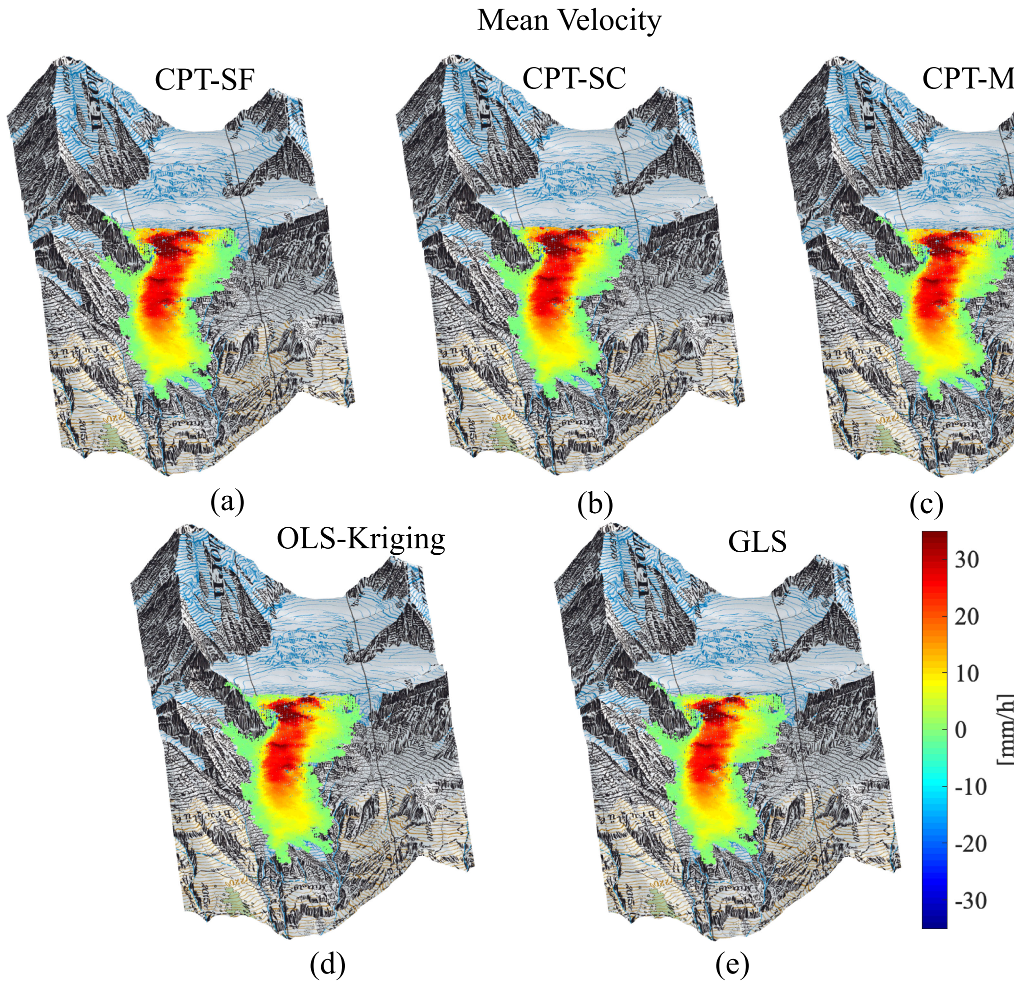

Fig. 15. Mean LOS velocity results derived by TRI images from 08:00 13th to 00:00, 16th July. (a) CPT-SF. (b) CPT-SC. (c) CPT-M. (d) OLS-kriging. (e) GLS.

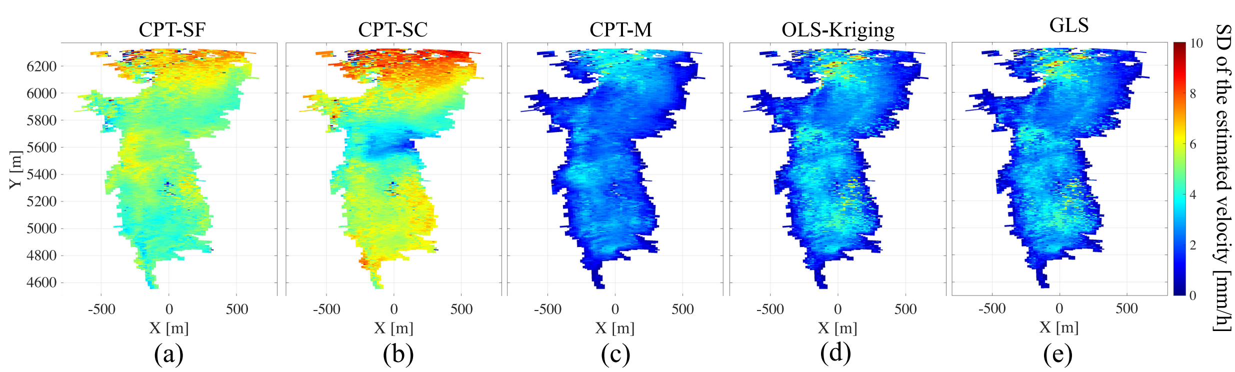

Fig. 16. SD of the estimated velocity derived by TRI images from 08:00 13th to 00:00, 16th July. (a) CPT-SF. (b) CPT-SC. (c) CPT-M. (d) OLS-kriging. (e) GLS.

and S_2 (outer part) points and corresponding time series results for three methods in Fig. 13.

The SD maps in Fig. 16 show similar results among the three methods over the glacier tongue. The same consequence is also given from the estimated velocity time series in Fig. 17(a) and (b), where the time series of the CPT-M is in agreement with geostatistical approaches.

When the contribution of the temporal covariance $\mathbf{\Sigma}_{\mathrm{APS,\,t}}$ in (25) is significant, the GLS inversion is advisable rather than the OLS-kriging as the solution gives us minimum variance and unbiased estimation. Nonetheless, the daisy chain adopted in our processing for interferogram pair selection makes diagonal variances of $\mathbf{\Sigma}_{\mathrm{APS,\,t}}$ constant (i.e., homoscedasticity) and does not show a high correlation among the

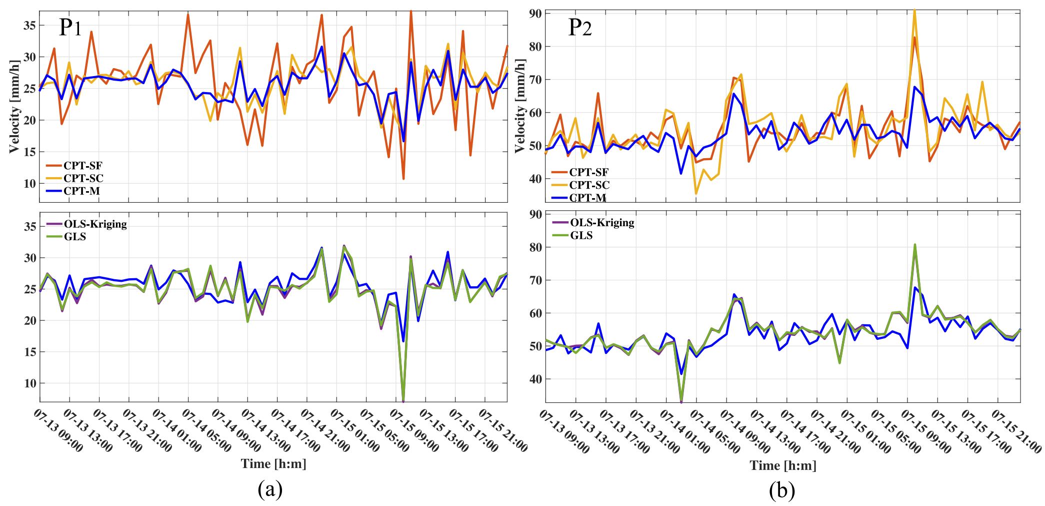

Fig. 17. Time series plots of the estimated LOS velocity at selected pixels on the glacier tongue. (a) P_1. (b) P_2.

interferograms (i.e., off-diagonal covariances of the $\mathbf{\Sigma}_{\mathrm{APS,\ t}}$ are expected to be close to zero) because selected interferograms according to the daisy chain do not share a reference image. Moreover, because the processing chain only uses the CPs for velocity retrieval, the covariance of decorrelation $\mathbf{\Sigma}_{\mathrm{decorr}}$ in (24) is expected to be close to zero. Due to such specific measurement conditions, the difference in performance between OLS-kriging and GLS appeared not significant in our analysis.

C. Advantageous Implications and Expected Applications of the Proposed Approach

Although the CPT-M proves to be an efficient estimation toward mitigating atmospheric disturbances, the exact knowledge of displacement location is required for the CPT-M as well as for geostatistical approaches. Nevertheless, the displacement location is often known in many applications. In the glacier measurement, a visual inspection may permit us the boundary detection of the moving part. Moreover, the data-driven moving area detection approach can be employed in a more robust manner. We observed that the glacier tongue showed a different scattering mechanism and a temporal scattering behavior from other regions over the cliff [63]. The temporal variation of the dielectric constant and the physical movement over the glacier tongue cause an amplitude variation and temporal decorrelation. Such characteristics lead to distinctive patterns of the glacier tongue from other regions. Therefore, several analyses, such as polarimetric target decomposition, DA, and interferometric absolute coherence, realize automatic glacier zone detection.

Finally, the CPT-M yielded almost identical accuracy to geostatistical methods with a lower computational cost. This advantage is especially significant in near-real-time monitoring. Recently, there is an increasing interest in multiple-input multiple-output (MIMO) radar for displacement monitoring [12], [64]. The MIMO radar allows fast acquisition of SAR images realized by the antenna array without physical movement of antennas; hence, it realizes real-time displacement monitoring. The proposed APS mitigation approach is expected to be suited to such an operation, supporting the fast generation of accurate displacement time series.

VIII. Conclusion

The presented work proposes an efficient approach for APS mitigation in differential radar interferometry based on the CPT velocity estimation algorithm.

The turbulent APS spatial behavior of our TRI dataset observed over the Bisgletscher is stochastically analyzed. The analysis reveals that the spatial statistic of the presented turbulent APS obeys a scale variant power low behavior. It also shows a temporal variation of the variance and the correlation length of the turbulence and reveals higher disturbance during the daytime than night-time.

A piecewise processing chain is introduced for the estimation of arbitrary temporal displacement patterns in this work. The introduced processing chain estimates the displacement velocity of each image subset, reconstructing arbitrary temporal displacement time series by linking all the results of subsets. A daisy chain is adopted in this processing chain to minimize temporal decorrelation and phase wrapping. The residual APS, which is the residual term after correction of the stratified APS, is further taken into account in the proposed approach.

A multiple-seed setting strategy is proposed as an add-on to the CPT algorithm toward mitigating residual APS. With *a priori* knowledge of displacement area, the proposed approach defines all CPs closest to the displacement pixels as seeds surrounding the moving area. An analysis by generated 2-D isotropic zero-mean Gaussian random fields reveals that the multiple-seed approach reduces the APS contribution on velocity estimation than single-seed cases. Moreover, the analysis shows that the variance and correlation length of the simulated turbulence limit the accuracy of the approach.

A case study of the glacier displacement measurement is carried out. The applicability of the proposed approach is tested with real TRI images acquired by KAPRI. The following consequences are obtained from the analysis through the comparison with different approaches.

1) The proposed approach reveals higher estimation accuracy and robustness than the CPT with a single seed. A multiple-seed setting effectively suppresses the residual APS accumulation effect at the integration step in the CPT.
2) The estimation accuracy of the proposed approach is almost as good as geostatistical approaches, i.e., the OLS-kriging and the GLS.

A noteworthy advantage of the proposed approach is its computational efficiency with a reasonable accuracy, which is considered as a proper APS mitigation for near-real-time operation.

Appendix

A. Stratified APS Compensation

According to (1) and (2), it is understood that modeling of N_{ref} will give the solution of $\phi_{\mathrm{APS,str}}$. Among the methods developed so far, we apply the model-based approach proposed in [43] in order to take into account the spatial heterogeneous N_{ref}. The distribution of the N_{ref} is described by quadratic 2-D polynomial function with respect to a topographic height and a slant range. The unwrapped stratified APS model is then defined by means of relative slant range distance r_s and topographic height z_d from radar location to position of interest, given by

$$\begin{aligned}&\phi_{\mathrm{APS,str}}\left(t_i, t_{i+1}\right)\\&= \beta_0 + \beta_1 r_s + \beta_2 r_s z_d + \beta_3 r_s {z_d}^2 + \beta_4 {r_s}^2 \\&\quad + \beta_5 {r_s}^3 + \beta_6 {r_s}^2 z_d\\&= \beta_0 + \beta_1 x_1 + \beta_2 x_2 + \beta_3 x_3 + \beta_4 x_4 + \beta_5 x_5 + \beta_6 x_6\end{aligned} \tag{15}$$

where $\beta_0, \ldots, \beta_6$ are the unknown parameters, and the β_0 shows the offset, $x_1, \ldots, x_6$ are observation variables. The matrix notation of (15) dealing with all the *k* candidates of pixels for estimation is given as

$$\phi = \mathbf{X}\boldsymbol{\beta} + \varepsilon, \tag{16}$$

where $\boldsymbol{\phi}$ is a [$k \times 1$] vector of measured interferometric phase, $\boldsymbol{\beta}$ is a [7×1] dimension vector of the unknown parameters, $\mathbf{X}$ is a [$k \times 7$] dimension vector of observation variables. The OLS inversion solves the unknown parameters $\boldsymbol{\beta}$ as [26]

$$\hat{\boldsymbol{\beta}} = \left(\mathbf{X}^T\mathbf{X}\right)^{-1}\mathbf{X}^T\boldsymbol{\phi}. \tag{17}$$

Finally, the estimated unknown parameters are substituted to (16) and the stratified APS can be estimated as

$$\hat{\boldsymbol{\phi}}_{\mathrm{APS,str}} = \mathbf{X}\hat{\boldsymbol{\beta}}. \tag{18}$$

The observation variables in (17) should be chosen from the CPs unaffected by displacement contribution because the inclusion of moving pixels consequently leads to bias estimates. Therefore, we exclude the glacier parts from the selected CPs for unknown parameter estimation in (17).

It is important to highlight that the selected *k* CPs must be spatially unwrapped before the inversion to make the system in (16) linear. In practice, only sparse points out of all CPs can be used in the estimation because the stratified APS usually shows large-scale variation. By doing so, there is no need to perform the phase unwrapping for all CPs, and hence the computational cost is not regarded as significant.

B. Pixel-Wise Velocity Inversion

A signal model of the interferometric phase is expressed as a matrix form allowing all *q* candidate pixels as

$$\overline{\boldsymbol{\phi}} = \overline{\mathbf{B}}\,\overline{\mathbf{v}} + \varepsilon, \tag{19}$$

where $\overline{\boldsymbol{\phi}} = \mathbf{I}_{q,1} \otimes \boldsymbol{\phi}_{\boldsymbol{x}}$ ($\boldsymbol{\phi}_{\boldsymbol{x}}$ is [$M \times 1$] vector of interferometric phases at pixel $\mathbf{x}$, and $\mathbf{I}_{q,1}$ is a [$q \times 1$] identity matrix), $\overline{\mathbf{v}} = \mathbf{I}_{q,1} \otimes \mathbf{v}_{\boldsymbol{x}}$ ($\mathbf{v}_{\boldsymbol{x}}$ is the [$N \times 1$] vector of velocities), ε is a noise-like component. $\overline{\mathbf{B}}$ is the block diagonal matrix [$qM \times qN$] computed by $\mathbf{I}_{q,q} \otimes \mathbf{B}$, and $\mathbf{B}$ is an [$M \times N$] matrix. In the daisy chain, $\mathbf{B}$ becomes

$$\mathbf{B} = \frac{4\pi}{\lambda}\begin{bmatrix} T_1 & 0 & 0 & \cdots & 0\\ 0 & T_2 & 0 & \cdots & 0\\ \vdots & \vdots & \vdots & \ddots & \vdots\\ 0 & 0 & 0 & T_M & 0\end{bmatrix}, \tag{20}$$

where T_i indicates the time interval between reference and secondary SLC images (all must be 2.5 min in this study). Since the condition becomes $M < N$ in this case, the rank of $\mathbf{B}$ becomes deficient, and no unique solution can be found for $\overline{\mathbf{v}}$ [16], [33]. By constraining the constant velocity assumption of $\mathbf{v}$ overtime as $\mathbf{v} = \mathbf{I}_{N,1} \cdot \mathbf{p}_{\boldsymbol{x}}$ where $\mathbf{p}_{\boldsymbol{x}} = v_0\left(\mathbf{x}\right)$, a system in (19) can be rewritten as

$$\overline{\boldsymbol{\phi}} = \overline{\mathbf{G}}\,\mathbf{p} + \varepsilon, \tag{21}$$

where $\overline{\mathbf{G}} = \overline{\mathbf{B}} \cdot \left(\mathbf{I}_{q,q} \otimes \mathbf{I}_{N,1}\right)$, $\mathbf{p}$ is [$q \times 1$] vector of constant velocity for all pixel candidates. The system in (21) now can be solved by OLS solution under linear system assumption as

$$\hat{\mathbf{p}}_{\mathrm{OLS}} = \left(\overline{\mathbf{G}}^T\overline{\mathbf{G}}\right)^{-1}\overline{\mathbf{G}}^T\overline{\boldsymbol{\phi}}. \tag{22}$$

When the noise term in (21) is correlated both in time and space and/or indicating heteroscedasticity (varying variance), GLS estimation can give the best linear unbiased estimator as [65]

$$\hat{\mathbf{p}}_{\mathrm{GLS}} = \left(\overline{\mathbf{G}}^T\boldsymbol{\Sigma}_{\phi}{}^{-1}\overline{\mathbf{G}}\right)^{-1}\overline{\mathbf{G}}^T\boldsymbol{\Sigma}_{\phi}{}^{-1}\overline{\boldsymbol{\phi}}, \tag{23}$$

where $\boldsymbol{\Sigma}_{\phi}$ is the [$qM \times qM$] covariance matrix of interferometric phase noise contributions, assumed to be the zero-mean Gaussian random process. Two noise terms of the residual APS and temporal decorrelation mainly degrade the signal quality. Thanks to the different physical mechanisms between APS and decorrelation, as well as linearity, the covariance matrix can be decomposed into residual APS $\boldsymbol{\Sigma}_{\mathrm{APS}}$ and decorrelation term $\boldsymbol{\Sigma}_{\mathrm{decorr}}$ as

$$\boldsymbol{\Sigma}_{\phi} = \boldsymbol{\Sigma}_{\mathrm{APS}} + \boldsymbol{\Sigma}_{\mathrm{decorr}}. \tag{24}$$

An effective treatment under the assumption of separability is applied to $\boldsymbol{\Sigma}_{\mathrm{APS}}$ for simplifying the statistic model in (24), where the separability implies that the spatial statistic is not a function of time [16]. Under this assumption, the APS covariance $\mathbf{\Sigma}_{\mathrm{APS}}$ can be further separated as a Kronecker product of spatial covariance $\mathbf{\Sigma}_{\mathrm{atm,\ s}}$ and temporal covariance $\mathbf{\Sigma}_{\mathrm{atm,\ t}}$ of SLC phases [16]

$$\begin{aligned}\mathbf{\Sigma}_{\mathrm{APS}} &= \mathbf{\Sigma}_{\mathrm{atm,\ s}} \otimes \left(\mathbf{A}_{\mathrm{infero}}\mathbf{\Sigma}_{\mathrm{atm,\ t}}\mathbf{A}_{\mathrm{infero}}{}^{T}\right)\\ &= \mathbf{\Sigma}_{\mathrm{atm,\ s}} \otimes \mathbf{\Sigma}_{\mathrm{APS,\ t}},\end{aligned} \tag{25}$$

where the $\mathbf{A}_{\mathrm{infero}}$ is $[M \times N]$ incidence matrix representing the interferometric combinations.

Although a large covariance matrix needs to be taken into account for the velocity inversion, a *simple kriging* (SK) interpolation can correct the spatial correlation of residual APS. Note that the method in [16] employed a *regression kriging* for the simultaneous estimation of the stratified APS and the residual APS. When the stratified APS has already been corrected, the SK can be applied assuming zero-mean over the field. Kriging interpolation predicts the residual APS by a weighted average of the local APS. In the kriging method, the weights are determined by the covariance of the spatial variables through the kriging system. The spatial prediction of unobserved residual APS by the SK at the arbitrary location $\mathbf{x}_0$ of ith interferogram is given as [53]

$$\hat{\phi}^{i}_{\mathrm{resAPS}}\left(\mathbf{x}_0\right) = C^{i}_{0}T\, C^{i}_{\alpha}\phi^{i}_{\mathrm{res,\ neighbor}}, \tag{26}$$

where C^{i}_{0} is an $[n \times 1]$ spatial APS covariance vector between $\mathbf{x}_0$ and n neighbor CPs, C^{i}_{α} is an $[n \times n]$ covariance matrix of n neighbor CPs, and $\phi^{i}_{\mathrm{res,\ neighbor}}$ is the observed APS over the n neighbor CPs. The covariance values in (26) are inferred from the fitted exponential variogram model in this study according to experimental variogram measured over the motionless CPs [66] using the following relationship under the second-order stationarity:

$$C\ (h) = \gamma_{\exp}\ (\infty) - \gamma\,(h)\,, \tag{27}$$

where $\gamma_{\exp}(\infty)$ corresponds to the sill value (variance). Note that the relationship in (27) is only valid when the variogram is bounded by a finite value.

Finally, the predicted APS is subtracted from the interferogram to correct the spatial correlation. In this way, $\mathbf{\Sigma}_{\mathrm{atm,\ s}}$ consequently becomes an identity matrix, resulting in the simplification of the covariance model in (25).

The remaining temporal covariance $\mathbf{\Sigma}_{\mathrm{atm,\ t}}$ is inferred through the estimation of the temporal variogram model using all pairs of interferogram images $N(N-1)/2$. The exponential variogram model is also employed for the temporal covariance inference. Finally, decorrelation covariance $\mathbf{\Sigma}_{\mathrm{decorr}}$ is obtained based on the exponential decay model of the temporal decorrelation (see step-by-step $\mathbf{\Sigma}_{\mathrm{decorr}}$ estimation in [23]).

Acknowledgment

The authors would like to thank Dr. Jan Beutel for providing the high-alpine wireless communication infrastructure and his support during the radar measurement campaign as the PermaSense/X-Sense project. The authors would also like to thank Marcel Stefko of ETH Zürich for his fruitful advice on data processing. The topographic map used in this work is from Swisstopo. The datasets and photographs in this article were acquired and were provided by the Chair of Earth Observation and Remote Sensing, ETH Zürich.

References

[1] D. Tarchi *et al.*, "On the use of ground-based SAR interferometry for slope failure early warning: The cortenova rock slide (Italy)," in *Landslides*, Berlin, Germany: Springer, 2005, pp. 337–342.

[2] G. Luzi, "Ground based SAR interferometry: A novel tool for geoscience," in *Geoscience and Remote Sensing New Achievements*, P. Imperatore and D. Riccio, Eds. London, U.K.: IntechOpen, 2010, pp. 1–28.

[3] Y. Wang *et al.*, "Ground-based differential interferometry SAR: A review," *IEEE Geosci. Remote Sens. Mag.*, vol. 8, no. 1, pp. 43–70, Mar. 2020.

[4] M. Pieraccini and L. Miccinesi, "Ground-based radar interferometry: A bibliographic review," *Remote Sens.*, vol. 11, no. 9, 2019, Art. no. 1029.

[5] D. Tarchi *et al.*, "Landslide monitoring by using ground-based SAR interferometry: An example of application to the Tessina landslide in Italy," *Eng. Geol.*, vol. 68, no. 1/2, pp. 15–30, Feb. 2003.

[6] K. Takahashi, M. Matsumoto, and M. Sato, "Continuous observation of natural-disaster-affected areas using ground-based SAR interferometry," *IEEE J. Sel. Top. Appl. Earth Observ. Remote Sens.*, vol. 6, no. 3, pp. 1286–1294, Jun. 2013.

[7] D. Leva, G. Nico, D. Tarchi, and J. Fortuny-Guasch, "Temporal analysis of a landslide by means of a ground-based SAR interferometer," *IEEE Trans. Geosci. Remote Sens.*, vol. 41, no. 4, pp. 745–752, Apr. 2003.

[8] J. Severin, E. Eberhardt, L. Leoni, and S. Fortin, "Development and application of a pseudo-3D pit slope displacement map derived from ground-based radar," *Eng. Geol.*, vol. 181, pp. 202–211, 2014.

[9] C. Hu, Y. Deng, W. Tian, and J. Wang, "A PS processing framework for long-term and real-time GB-SAR monitoring," *Int. J. Remote Sens.*, vol. 40, no. 16, pp. 6298–6314, 2019.

[10] A. Montuori *et al.*, "The interferometric use of radar sensors for the urban monitoring of structural vibrations and surface displacements," *IEEE J. Sel. Top. Appl. Earth Observ. Remote Sens.*, vol. 9, no. 8, pp. 3761–3776, Aug. 2016.

[11] D. Tarchi, H. Rudolf, G. Luzi, L. Chiarantini, P. Coppo, and A. J. Sieber, "SAR interferometry for structural changes detection: A demonstration test on a dam," in *Proc. IEEE Int. Geosci. Remote Sens. Symp.*, 1999, pp. 1522–1524.

[12] M. Pieraccini and L. Miccinesi, "An interferometric MIMO radar for bridge monitoring," *IEEE Geosci. Remote Sens. Lett.*, vol. 16, no. 9, pp. 1383–1387, Sep. 2019.

[13] G. Nico, G. Prezioso, O. Masci, and S. Artese, "Dynamic modal identification of telecommunication towers using ground based radar interferometry," *Remote Sens.*, vol. 12, no. 7, 2020, Art. no. 1211.

[14] F. Pratesi *et al.*, "Early warning GBInSAR-based method for monitoring volterra (Tuscany, Italy) city walls," *IEEE J. Sel. Top. Appl. Earth Observ. Remote Sens.*, vol. 8, no. 4, pp. 1753–1762, Apr. 2015.

[15] M. Pieraccini *et al.*, "Radar detection of pedestrian-induced vibrations on Michelangelo's David," *PLoS One*, vol. 12, no. 4, 2017, Art. no. e0174480.

[16] S. Baffelli, O. Frey, and I. Hajnsek, "Geostatistical analysis and mitigation of the atmospheric phase screens in ku-band terrestrial radar interferometric observations of an alpine glacier," *IEEE Trans. Geosci. Remote Sens.*, vol. 58, no. 11, pp. 7533–7556, Apr. 2020.

[17] G. Luzi *et al.*, "Monitoring of an alpine glacier by means of ground-based SAR interferometry," *IEEE Geosci. Remote Sens. Lett.*, vol. 4, no. 3, pp. 495–499, Jul. 2007.

[18] N. Dematteis, G. Luzi, D. Giordan, F. Zucca, and P. Allasia, "Monitoring Alpine glacier surface deformations with GB-SAR," *Remote Sens. Lett.*, vol. 8, no. 10, pp. 947–956, 2017.

[19] H. Chai, X. Lv, and P. Xiao, "Deformation monitoring using ground-based differential SAR tomography," *IEEE Geosci. Remote Sens. Lett.*, vol. 17, no. 6, pp. 993–997, Jun. 2020.

[20] A. Martinez-Vazquez and J. Fortuny-Guasch, "A GB-SAR processor for snow avalanche identification," *IEEE Trans. Geosci. Remote Sens.*, vol. 46, no. 11, pp. 3948–3956, Nov. 2008.

[21] L. Liu, L. Jiang, Y. Sun, H. Wang, Y. Sun, and H. Xu, "Diurnal fluctuations of glacier surface velocity observed with terrestrial radar interferometry at Laohugou no. 12 glacier, Western Qilian Mountains, China," *J. Glaciology*, vol. 65, no. 250, pp. 239–248, 2019.

[22] L. D. Euillades *et al.*, "Detection of glaciers displacement time-series using SAR," *Remote Sens. Environ.*, vol. 184, pp. 188–198, 2016.

[23] P. S. Agram and M. Simons, "A noise model for InSAR time series," *J. Geophysical Res.: Solid Earth*, vol. 120, no. 4, pp. 2752–2771, Apr. 2015.

[24] R. Jolivet *et al.*, "Improving InSAR geodesy using global atmospheric models," *J. Geophysical Res.: Solid Earth*, vol. 119, no. 3, pp. 2324–2341, 2014.
[25] Z. Li *et al.*, "Time-series InSAR ground deformation monitoring: Atmospheric delay modeling and estimating," *Earth Sci. Rev.,* vol. 192, pp. 258–284, 2019.
[26] R. Iglesias *et al.*, "Atmospheric phase screen compensation in ground-based SAR with a multiple-regression model over mountainous regions," *IEEE Trans. Geosci. Remote Sens.*, vol. 52, no. 5, pp. 2436–2449, May 2014.
[27] J. Dong, L. Zhang, M. Liao, and J. Gong, "Improved correction of seasonal tropospheric delay in InSAR observations for landslide deformation monitoring," *Remote Sens. Environ.*, vol. 233, 2019, Art. no. 111370.
[28] V. I. Tatarski, *Wave Propagation in a Turbulent Medium*. New York, NY, USA: Dover Publications, 1961.
[29] R. F. Hanssen, *Radar Interferometry: Data Interpretation and Error Analysis*. Dordrecht, The Netherlands: Kluwer, 2001.
[30] M. Crosetto, O. Monserrat, M. Cuevas-González, N. Devanthéry, and B. Crippa, "Persistent scatterer interferometry: A review," *ISPRS J. Photogrammetry Remote Sens.*, vol. 115, pp. 78–89, 2016.
[31] A. Ferretti, C. Prati, and F. Rocca, "Permanent scatterers in SAR interferometry," *IEEE Trans. Geosci. Remote Sens.*, vol. 39, no. 1, pp. 1528–1530, Jan. 2001.
[32] A. Ferretti, C. Prati, and F. Rocca, "Nonlinear subsidence rate estimation using permanent scatterers in differential SAR interferometry," *IEEE Trans. Geosci. Remote Sens.*, vol. 38, no. 5, pp. 2202–2212, Sep. 2000.
[33] P. Berardino, G. Fornaro, R. Lanari, and E. Sansosti, "A new algorithm for surface deformation monitoring based on small baseline differential SAR interferograms," *IEEE Trans. Geosci. Remote Sens.*, vol. 40, no. 11, pp. 2375–2383, Nov. 2002.
[34] O. Mora, J. J. Mallorqui, and A. Broquetas, "Linear and nonlinear terrain deformation maps from a reduced set of interferometric SAR images," *IEEE Trans. Geosci. Remote Sens.*, vol. 41, no. 10, pp. 2243–2253, Oct. 2003.
[35] P. Blanco-Sánchez, J. J. Mallorquí, S. Duque, and D. Monells, "The coherent pixels technique (CPT): An advanced DInSAR technique for nonlinear deformation monitoring," *Pure Appl. Geophys.*, vol. 165, no. 6, pp. 1167–1193, 2008.
[36] R. Iglesias *et al.*, "Ground-based polarimetric SAR interferometry for the monitoring of terrain displacement phenomena - Part I: Theoretical description," *IEEE J. Sel. Top. Appl. Earth Observ. Remote Sens.*, vol. 8, no. 3, pp. 980–993, Mar. 2015.
[37] Z. Wang, Z. Li, and J. Mills, "A new approach to selecting coherent pixels for ground-based SAR deformation monitoring," *ISPRS J. Photogrammetry Remote Sens.*, vol. 144, pp. 412–422, 2018.
[38] L. Pipia *et al.*, "Polarimetric differential SAR interferometry : First results with ground-based measurements," *IEEE Geosci. Remote Sens. Lett.*, vol. 6, no. 1, pp. 167–171, Jan. 2009.
[39] G. Nico, R. Tome, J. Catalao, and P. M. A. Miranda, "On the use of the WRF model to mitigate tropospheric phase delay effects in SAR interferograms," *IEEE Trans. Geosci. Remote Sens.*, vol. 49, no. 12, pp. 4970–4976, Dec. 2011.
[40] P. Mateus, G. Nico, and J. Catalao, "Uncertainty assessment of the estimated atmospheric delay obtained by a numerical weather model (NMW)," *IEEE Trans. Geosci. Remote Sens.*, vol. 53, no. 12, pp. 6710–6717, Dec. 2015.
[41] L. Pipia, X. Fàbregas, A. Aguasca, and C. López-Martínez, "Atmospheric artifact compensation in ground-based DInSAR applications," *IEEE Geosci. Remote Sens. Lett.*, vol. 5, no. 1, pp. 88–92, Jan. 2008.
[42] L. Noferini *et al.*, "Using GB-SAR technique to monitor slow moving landslide," *Eng. Geol.*, vol. 95, no. 3/4, pp. 88–98, 2007.
[43] Y. Izumi, L. Zou, K. Kikuta, and M. Sato, "Iterative atmospheric phase screen compensation for near-real-time ground-based In SAR measurements over a mountainous slope," *IEEE Trans. Geosci. Remote Sens.*, vol. 58, no. 8, pp. 5955–5968, Aug. 2020.
[44] J. Liu, H. Yang, L. Xu, and T. Li, "Novel model-based approaches for non-homogenous atmospheric compensation of GB-InSAR in the Azimuth and horizontal directions," *Remote Sens.,* vol. 13, no. 11, May 2021, Art. no. 2153.
[45] A. Karunathilake and M. Sato, "Atmospheric phase compensation in extreme weather conditions for ground-based SAR," *IEEE J. Sel. Top. Appl. Earth Observ. Remote Sens.*, vol. 13, pp. 3806–3815, Jun. 2020.
[46] Y. Izumi, L. Zou, K. Kikuta, and M. Sato, "Anomalous atmospheric phase screen compensation in ground-based SAR over mountainous area," in *Proc. Int. Geosci. Remote Sens. Symp.*, 2019, pp. 2030–2033.
[47] J. Butt, A. Wieser, and S. Conzett, "Intrinsic random functions for mitigation of atmospheric effects in terrestrial radar interferometry," *J. Appl. Geodesy*, vol. 11, no. 2, pp. 89–98, 2017.
[48] S. Baffelli, O. Frey, C. Werner, and I. Hajnsek, "System characterization and polarimetric calibration of the ku-band advanced polarimetric interferometer," in *Proc. Eur. Conf. Synth. Aperture Radar*, 2016, pp. 1–6.
[49] S. Baffelli, O. Frey, C. Werner, and I. Hajnsek, "Polarimetric calibration of the ku-band advanced polarimetric radar interferometer," *IEEE Trans. Geosci. Remote Sens.*, vol. 56, no. 4, pp. 2295–2311, Apr. 2018.
[50] C. Werner, A. Wiesmann, T. Strozzi, A. Kos, R. Caduff, and U. Wegmuller, "The GPRI multi-mode differential interferometric radar for ground-based observations," in *Proc. Eur. Conf. Synthetic Aperture Radar*, 2012, pp. 304–307.
[51] S. Liu, "Satellite radar interferometry: Estimation of atmospheric delay," Ph.D. dissertation, Geosci. Remote Control Dept., Delft Univ. Technol., Delft, The Netherlands, 2013.
[52] R. B. Stull and C. D. Ahrens, *Meteorology Today for Scientists and Engineers*. West Pub., St. Paul, Minneapolis, 1995.
[53] H. Wackernagel, *Multivariate Geostatistics*. Berlin, Germany: Springer, 1998.
[54] S. H. Hong, S. Wdowinski, S. W. Kim, and J. S. Won, "Multi-temporal monitoring of wetland water levels in the Florida everglades using interferometric synthetic aperture radar (InSAR)," *Remote Sens. Environ.*, vol. 114, no. 11, pp. 2436–2447, 2010.
[55] B. Osmanoğlu, F. Sunar, S. Wdowinski, and E. Cabral-Cano, "Time series analysis of InSAR data: Methods and trends," *ISPRS J. Photogrammetric Remote Sens.*, vol. 115, pp. 90–102, 2016.
[56] M. R. Hestenes and E. Stiefel, "Methods of conjugate gradients for solving linear systems," *J. Res. Nat. Bur. Standards*, vol. 49, no. 6, pp. 409–435, 1952.
[57] G. Centolanza, "Quality evaluation of DInSAR results from the phase statistical analysis," Ph.D. dissertation, Departament de Teoria del Senyal i Comunicacions, Universitat Polit'ecnica de Catalunya (UPC), Barcelona, Spain, 2015.
[58] M. Schlather, "Construction of covariance functions and unconditional simulation of random fields," in *Advances and Challenges in Space-Time Modelling of Natural Events*, Berlin, Germany: Springer, 2012, pp. 25–54.
[59] C. R. Dietrich and G. N. Newsam, "A fast and exact method for multidimensional Gaussian stochastic simulations," *Water Resour. Res.*, vol. 29, no. 8, pp. 2861–2869, 1993.
[60] M. Schlather, "Simulation and analysis of random fields," *R News*, vol. 1, no. 2, pp. 18–20, 2001.
[61] M. Costantini, "A novel phase unwrapping method based on network programming," *IEEE Trans. Geosci. Remote Sens.*, vol. 36, no. 3, pp. 813–821, May 1998.
[62] S. Conzett, A. Wieser, and J. A. Butt, "Exploiting amplitude of terrestrial radar data for feature tracking in areal monitoring of inhomogeneous surfaces," in *Proc. 3rd Joint Int. Symp. Deformation Monit.*, pp. 1–11, 2016.
[63] S. Baffelli, O. Frey, and I. Hajnsek, "Polarimetric analysis of natural terrain observed with a ku-band terrestrial radar," *IEEE J. Sel. Top. Appl. Earth Observ. Remote Sens.*, vol. 12, no. 12, pp. 5268–5288, Dec. 2019.
[64] D. Tarchi, F. Oliveri, and P. F. Sammartino, "MIMO radar and ground-based SAR imaging systems: Equivalent approaches for remote sensing," *IEEE Trans. Geosci. Remote Sens.*, vol. 51, no. 1, pp. 425–435, Jan. 2013.
[65] T. Kariya and H. Kurata, *Generalized Least Squares*. West Sussex, U.K.: Wiley, 2004.
[66] J. P. Chilès and P. Delfiner, *Geostatistics: Modeling Spatial Uncertainty*, 2nd ed. Hoboken, NJ, USA: Wiley, 2012.

Yuta Izumi (Member, IEEE) received the B.Eng. and M.Eng. degrees in radar remote sensing from Chiba University, Chiba, Japan, in 2016 and 2018, respectively, and the Ph.D. degree in radar remote sensing from the Tohoku University, Sendai, Japan, in 2021.

He is currently a JSPS Research Fellow PD with the Institute of Industrial Science, University of Tokyo, Tokyo, Japan. His research interests include SAR interferometry and polarimetry and their applications for disaster mitigation.

Dr. Izumi was the recipient of the Young Researcher Award from the IEEE Geoscience and Remote Sensing Society All Japan Joint Chapter.

Othmar Frey (Senior Member, IEEE) received the M.Sc. degree in geomatic engineering from ETH Zürich, Zürich, Switzerland, in 2002 and the Ph.D. (Dr.sc.nat.) degree in radar remote sensing from the University of Zurich, Zürich, Switzerland, in 2010.

He is currently a Tenured Senior Scientist and a Lecturer with ETH Zürich and a Senior Scientist with GAMMA Remote Sensing AG, Switzerland. Since 2011, he has been working in this joint academic/industry setting. From 2002 to 2010, he was a Research Associate with the Remote Sensing Laboratory, University of Zurich. He has been a PI/Co-Investigator in various national and international research projects. At GAMMA, he has also been active in the development of the Gamma Software and in technical/scientific consulting on SAR imaging and interferometric applications to ESA, NASA, and aerospace industry. His research interests include 2-D and 3-D (tomographic) synthetic aperture radar imaging and interferometric/polarimetric techniques for applications such as 3-D forest mapping, ground deformation monitoring, and snow layer profiling using spaceborne, airborne, UAV-borne, and terrestrial radar sensors.

Dr. Frey is a Member of the SAOCOM-CS Science Expert Group, European Space Agency. Since 2015, he has been the Chair of the Swiss Chapter of the IEEE Geoscience and Remote Sensing Society. He was the recipient of the ETH Medal for his M.Sc. thesis and the Distinction Award and Prize from the Faculty of Science, University of Zurich.

Simone Baffelli (Member, IEEE) received the M.Sc. degree in electrical engineering and the Ph.D. degree from ETH Zurich, Zürich, Switzerland, in 2013 and 2018, respectively. His Ph.D. dissertation was on terrestrial radar interferometry.

He is currently a Postdoctoral Researcher with the Swiss Federal Laboratories for Materials Science and Technology, where he works on geostatistical analysis, sensor calibration, and data assimilation techniques for CarboSense, a Swiss-wide CO2 monitoring network. His research interests include remote sensing, particulary radar remote sensing, sensor network, data assimilation, and geostatistics.

Irena Hajnsek (Fellow, IEEE) received the Diploma degree (Hons.) in fluvial river systems from the Freie Universität Berlin, Berlin, Germany, in 1996 and the Dr. rer. nat. degree (Hons.) in model-based estimation of soil moisture from fully polarimetric synthetic aperture radar from the Friedrich Schiller University of Jena, Jena, Germany, in 2001.

Since November 2009, she has been a Professor of earth observation with the Institute of Environmental Engineering, Swiss Federal Institute of Technology and the head of the Polarimetric SAR Interferometry Research Group, German Aerospace Center Microwaves and Radar Institute. Her main research interests include electromagnetic propagation and scattering theory, radar polarimetry, SAR and interferometric SAR data processing techniques, and environmental parameter modelling and estimation. Since 2010, she has been the science coordinator of the German satellite mission TanDEM-X and proposed satellite mission Tandem-L.

Prof. Hajnsek is a Member of the European Space Agency Mission Advisory Group for the ROSE-L Mission. She was also the Technical Program Co-chair of the IEEE IGARSS 2012 in Munich, Germany, and Yokohama, Japan, in 2019. Since 2013, she has been a Member of the IEEE GRSS AdCom and from 2016 to 2020, she was the Vice President of the IEEE GRSS Technical Committees.

Motoyuki Sato (Fellow, IEEE) received the B.E., M.E, and Dr.Eng. degrees in information engineering from Tohoku University, Sendai, Japan, in 1980, 1982, and 1985, respectively.

Since 1997, he has been a Professor with Tohoku University, Sendai, Japan, and a Distinguished Professor of Tohoku University from 2007 to 2011, and the director of Center for Northeast Asian Studies, Tohoku University from 2009 to 2013. From 1988 to 1989, he was a Visiting Researcher with the Federal German Institute for Geoscience and Natural Resources, Hannover, Germany. He was a Visiting Professor with Jilin University, Changchun, China, the Delft University of Technology, Delft, The Netherlands, and the Mongolian University of Science and Technology, Ulan Bator, Mongolia. He developed GPR sensors for humanitarian demining, and they are used in mine affected countries including Cambodia. His current research interests include transient electromagnetics and antennas, radar polarimetry, ground penetrating radar, borehole radar, electromagnetic induction sensing, GB-SAR, and MIMO radar systems.

Dr. Sato was the recipient of the 2014 Frank Frischknecht Leadership Award from SEG for his contribution to his sustained and important contributions to near-surface geophysics in the field of ground-penetrating radar, the IEICE Best Paper Award in 2017 (Kiyasu Award) and 2020, the Achievement Award in 2019, the IEEE GRSS Education Award in 2012 and the IEEE Ulrich L. Rohde Innovative Conference Paper Awards on antenna measurements and applications in 2017. He was a Member of the IEEE GRSS AdCom from 2006 to 2014. He is a Chair of IEEE Sendai section in 2020–2021. He was an Associate Editor for the IEEE GEOSCIENCE AND REMOTE SENSING LETTERS, and the Guest Editor of the special issue of GPR2006 and GPR2010 in TRANSACTIONS ON GEOSCIENCE AND REMOTE SENSING, and IGARSS2011, GPR2012, and GPR2014 in IEEE JOURNAL OF SELECTED TOPICS IN APPLIED ERATH OBSERVATIONS AND REMOTE SENSING. He was the Chair of the IEEE GRSS Japan Chapter from 2006 to 2007. He was also the Technical Chair of GPR1996 in Sendai and the General Chair of IGARSS2011 Sendai-Vancouver.